D20.2
Improved aerodynamic, development & demonstration intermediate report No. 2

Project acronym:	Rail4EARTH
Starting date:	01/12/2022
Duration (in months):	48
Call (part) identifier:	
Grant agreement no:	101101917
Due date of deliverable:	Month 32
Actual submission date:	10/10/2025
Responsible/Author:	D. Heine / DLR
Dissemination level:	Public
Status:	Issued

Reviewed: yes

This project has received funding from the European Union's Horizon Europe research and innovation programme under Grant Agreement No 101101917.

Document history		
Revision	*Date*	*Description*
1	01.06.2025	First issue
2	01.09.2025	Reviewed issue
3	10.10.2025	First final version
4	??.??.2025	Revised version

Report contributors		
Name	Beneficiary Short Name	Details of contribution
E Allain	SNCF	Report writing
Y Brunaux	Wabtec	Review and Update of Report
U Fey	DLR	Report writing
D Heine	DLR	Report writing
M Iraeta	CAF	Report writing
T Kowalski	DLR	Report writing
F Moro	STS	Report writing
S Raiti	STS	Report writing
S Wallin	KTH	Report writing

Table of Contents

1. Executive Summary

This report shows the current status of work package 20 Aerodynamics. The work package consists of two tasks, whose content is strongly linked. The report give insight into the activities during the time span since the last report and also clarifies the future work until completion of the WP.

The first of the two tasks discusses the development of an accurate numerical method to predict the aerodynamic behaviour of a train model, in the second task the influence of two elements of a regional train on the aerodynamic is examined, namely the train roof components and the pantograph.

One main aim of the work package is to establish a prediction method for aerodynamic loads on a regional train. In task 20.1 the methods, which were identified to be promising in the last report, were used to evaluate the flow in the simulated, generic wind tunnel with different stages of refinement and granularity. The different methods were implemented by the partners which usually use these specific methods so that the results can be compared and an optimized method can be implemented. For validation experimental tests in model scale are performed to set up a database with a variation of train roof components. As comparison parameter, the drag of the generic regional train KMF regio introduced in the first deliverable was tested and the numerical and experimental results will be compared.

In the task 20.2.1, the drag of the KMF train shall be reduced by means of the variation of roof installations. A variety of roof configurations was already introduced; these variations will now be tested experimentally in the wind tunnel and selected configurations will be studied with the different numerical codes. Aim of the task 20.2.1 is the understanding of the development of drag due to flow structures at the train roof and to reduce this drag in order to enhance the ecological and financial performance of the train so to reduce fuel consumption and CO2 emission.

One of the possible roof installations of a train is the pantograph, whose aerodynamic behaviour is studied in task 20.2.2. The contact pressure between the pantograph and the power wire can be adjusted using aerodynamic guiding devices. By improving the aerodynamic characteristics of these pantograph components, the power transfer efficiency can be optimized and the abrasion of the wire and the pantograph can be reduced. Therefore, a generic, modular pantograph was designed and the model built in the scaling 1:1 to be studied in the wind tunnel.

By now, all tasks are according to the plan, no delays have to be reported.

2. Abbreviations and acronyms

Abbreviation / Acronym	Description
Beneficiaries	signatories of the GRANT AGREEMENT Project 101101917 — FP4 - Rail4EARTH
CFD	Computational Fluid Dynamics
Cmx,lee	Roll moment coefficient over leeside
ERJU	Europe's Rail Joint Undertaking
FP	ERJU Flagship Project
LES	Large Eddy Simulation
RANS	Reynolds Average Navier Stokes
SP	Sub-Project
SWG	Seitenwindkanal Göttingen (Crosswind Simulation Facility Göttingen)
WP	Work Package
WT	Wind tunnel

3. List of Figures

27	Drag coefficients for different parts (top) and cumulative drag (bottom) for the two geometries in wind tunnel with and w/o sword. Influence of turbulence models
28	Drag coefficients for different parts (top) and cumulative drag (bottom) for the two geometries in open conditions using SST. Influence of side wind
29	CFx comparison between CFD and WT results

4. List of tables

5. Background and Aim of the Work Package

Railway transportation is one of the safest and most ecological and means of transport which exists. This is, of course, a main part of the design process of new rail vehicles. The homologation process of a newly designed rail vehicles comprises the exterior aerodynamic according to the TSI LOC&PAS (for further information see [1]), in which regulations regarding the five topics slipstream effects, head pressure pulse, maximum pressure variation in tunnels, crosswind and ballast pick-up are stated. Within this WP, we focus on the main topics crosswind, which is part of the TSI LOC&PAS and on the running resistance of a train, which, on the first sight, is not regulated in the TSI. However, the certification of a new train set is regulated by the European standards, which are defined CEN TC256 WG06. The effective norm EN14067-6 regulates crosswind certification activities and defines the procedural methods to determine the crosswind loads on the train (see [2] for further insight). The norm EN14067-4 ([3]) gives a standard procedure to obtain the running resistance of the train set. The CEN work group defined a guide for the use of simulations for the applications above (see [4]).

Although this is not required by TSI, the declaration of the running resistance is an essential information for the train operator, therefore, it is a required information during the buying process of the trains.

To obtain information about the running resistance, full-scale tests are required which are time- and cost-consuming and have an influence on the Life-cycle costs. Furthermore, the running-resistance of the train is essential for the energy consumption of the train.

Reduction of the train's running resistance will lead to a more energy-efficient transportation. Roof installations of the trains affect the running resistance, as they often cover a large area of the train and have sharp edges and surfaces, which are exposed to high wind speeds. Especially train components which outreach the train's boundary layer are significant as they are exposed to high wind speeds leading to serious wind resistance.

Within the WP20, two main activities are conducted:

- Task 20.1: numerical methodologies are identified, validated with exp. Tests and improved to accurately predict the wind resistance and the crosswind loads of a generic regional train
- Task 20.2: roof installations are tested numerically and experimentally to assess the influence of the position, shape and arrangement of the installations on the wind resistance as well as an optimization of a specific roof component (which was chosen to be the pantograph)

The goal of task 20.1 is to implement a numerical simulation tool of the train's

aerodynamic behaviour, so that this method can be advanced to a tool for virtual certification, so the effort for costly full-scale tests can be reduced. Within the task, different numerical tools are implemented and additional wind-tunnel tests with the same setup are conducted to gain a database for validation purposes.

The task 20.2 is divided into two subtasks, namely subtask 20.2.1 and 20.2.2. In the first subtask the positioning of the roof equipment is studied with the aim to reduce the overall drag of the train. The pantograph is investigated within the second subtask 20.2.2. The drag is to be reduced and exchangeable attachment parts will be adapted to optimize the contact pressure between the pantograph and the wire in order to ensure a high power transfer efficiency.

6. Link to KPI matrix

The topics of the WP interconnect with multiple KPIs baselines.
The main objective of the WP is to introduce a method to virtually certificate a train so to predict accurately the loads on the train for different train setups with the smallest effort possible. This would lead to a significantly decreased certification costs because of a low number of costly full-scale tests. Furthermore, critical aerodynamic behavior could be detected within the design process and not stated during the certification attempt leading to a smoother and faster way from first design to operable train. These factors will result in a decreased life-cycle costs of the vehicles.
The topics of task 20.2 will serve to optimizing the flow structures around the vehicle by changing the shape and arrangement of the roof installation devices. This shall lead to a reduced wind resistance of the train and therefore reduced fuel or physical energy consumption. Furthermore, due to reduced vortices, the noise emission is to be reduced.

7. Ongoing Work and Current Results

7.1. Scope of Work

The main scope of task 20.1 is to introduce a tool for simulating the flow around a train or a train model with moderate time and effort and maximal reliability and accuracy. In the future, certification of a train shall be done virtually with only a small number of full-scale tests so this numerical tool can help to pave the way for future certification methods.

Three different simulation methods were identified as potential certification tool. To test the capability of these tools, simulations of the flow around a generic, 1:20 scaled train model named KMF regio as a test object are performed. To validate the results, wind-tunnel tests are executed in the Crosswind Tunnel Göttingen SWG. The results obtained with the different tools are inspected with the main focus on the drag (so the wind resistance) and the crosswind loads on the train.

To get an idea of the influence of installations on the train roof on the overall drag of the train, a variety of roof configurations is tested in the wind tunnel as well as numerically. The configurations are designed in a way that the influence of the position of defined boxes can be studied plus the effect of the shape and size of the particular boxes. The definition of the roof configurations is scope of subtask 20.2.1.

As special case for roof installations, a generic and modular full-scale pantograph was designed within the scope of subtask 20.2.2 with the aim to study and optimize the aerodynamic behaviour of this roof component. The wind-tunnel tests are ongoing; therefore, this report focusses on task 20.1 and subtask 20.2.1.

Especially the topics of task 20.1 and subtask 20.2.1 strongly depend from one another as the simulation tool developed in task 20.1 is used in subtask 20.2.1 and the geometric setup designed in subtask 20.2.1 acts as test case in task 20.1. Therefore, the results overlap.

Within this report, the first results of the KMF regio simulations and WT tests are presented and compared.

7.2. Setup of Numerical Simulations

During 2025, the first CFD simulations have been carried out together with the first tunnel tests performed by DLR at the SWG wind tunnel Göttingen. The main objective of the performed wind tunnel tests is the evaluation of the aerodynamic drag for the KMF reference vehicle with different roof configurations. On the other hand, CFD

simulations aim to develop a methodology that allows a good correlation with the tunnel tests.

This section aims to describe the first simulation activities carried out during the time span since the last report. For this purpose, it is considered useful to follow the following structure which is closely related to the workflow adopted for the CFD simulations:

- Modelling of the wind tunnel
- Domain
- Vehicle model
- Boundary conditions
- Mesh
- Numerical parameters
- Results

In the following, each of the above mentioned sections will be discussed in more detail.

7.3. Modelling of the Wind Tunnel and Results of Simulations Performed with Method Proposed by KTH with Empty Wind Tunnel

The wind-tunnel setup is explained in detailed in the previous deliverable. For accurate comparison between CFD and measurements, the wind tunnel needs to be included within the CFD analysis with sufficient accuracy including the major considerations made for reducing the wind-tunnel installation effects such as the sword, the running floor and the suction panels. For this reason, we made a precursor CFD study of the empty wind tunnel with the major objective to be used for the upcoming CFD studies of the different configurations of the model mounted in the wind tunnel.

We made the choice of representing the wind-tunnel by the geometry that is formed by the contraction and the straight part (named Wind tunnel EdC | WT_C). The surrounding details including the suction channels were considered to add unnecessarily complexities which might introduce spurious numerical errors for the main study. The inlet contraction is, though, necessary for correct representation of the growing boundary layers on all the wind-tunnel walls, which is necessary for capturing the small but significant effective area contraction through the test section.

The mesh for the study was made using Pointwise as a hybrid mesh with structured surface mesh, boundary layer extrusion and a quad-dominated volume cell with a resolution of around 20mm in the volume and for the surface (wall) mesh. The wall-normal resolution is 0.01 and 0.2 mm for the wall resolved and wall-function boundary conditions respectively with an expansion (growth) coefficient of 1.15. The total number of grid points are 1.3 and 2.0 million respectively, see Fig. 1. It was verified that the (scalable) wall-function and wall resolved results were almost identical. Moreover, an overall mesh refinement showed no significant differences.

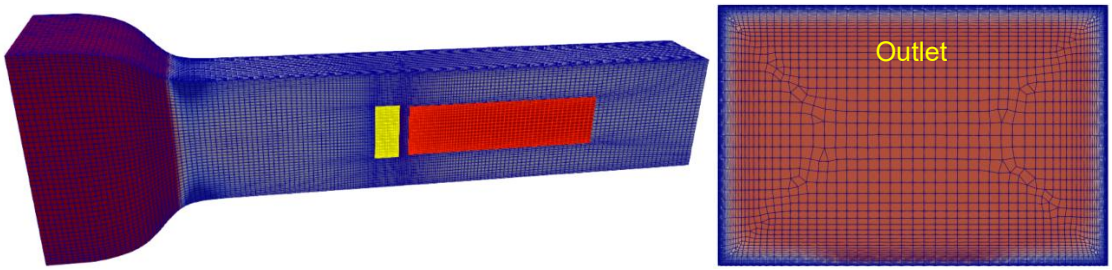

Fig. 1: mesh for the study of the wind-tunnel setup

The flow through the wind tunnel is driven by a total state inlet and a mass flow outlet (adapting the outlet static pressure) for the nominal condition at the test section of U=30m/s and p=1bar. Conditions are specified in Tab 1.

Tab. 1: CFD wind-tunnel conditions

Inlet total pressure, P_0	100522.0Pa
Inlet total temperature, T_0	300.0K
Outlet mass flow, $\dot{m}$	131.2kg/s
Test section pressure, p_∞	approx. 1.0e5Pa
Test section velocity, U_∞	approx. 30m/s
Inlet turbulence level, TI	0.3%
Inlet turbulence length scale, L_T	0.1m
Suction panel pressure, p_{sp}	99927Pa
Suction panel mass flow, $\dot{m}_{sp}$	1.91kg/s

Many different settings for the suction panel for correct inlet boundary layer around the position of the train head were tested. Two of these are reported in the following and shown in Fig 2. These are

- **Suction panel**: Representation of the suction panel as a pressure outlet boundary condition matching the measured suction mass flow.
- **Slip wall**: A simplified representation of the effect of the suction panel by applying a slip-wall boundary condition from the contraction to the position where the suction panel ends.

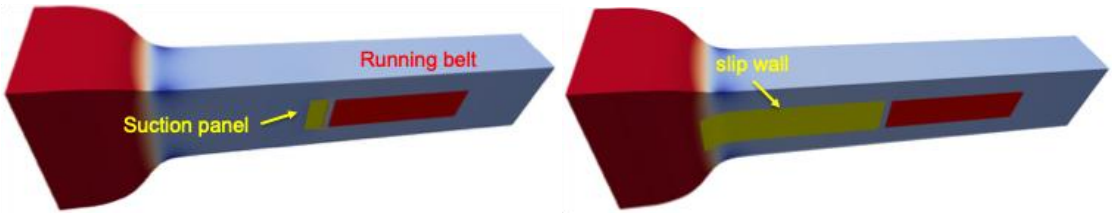

Fig. 2: Representation of the wind-tunnel suction by suction panel (left) and slip wall (right)

It is verified in Fig. 3 that the boundary layer is well captured by CFD when the belt is not running, and no suction is applied. The primary effect of the running belt and suction panel and the combination of these is shown for CFD, where the mitigation of the thick incoming boundary layer is demonstrated.

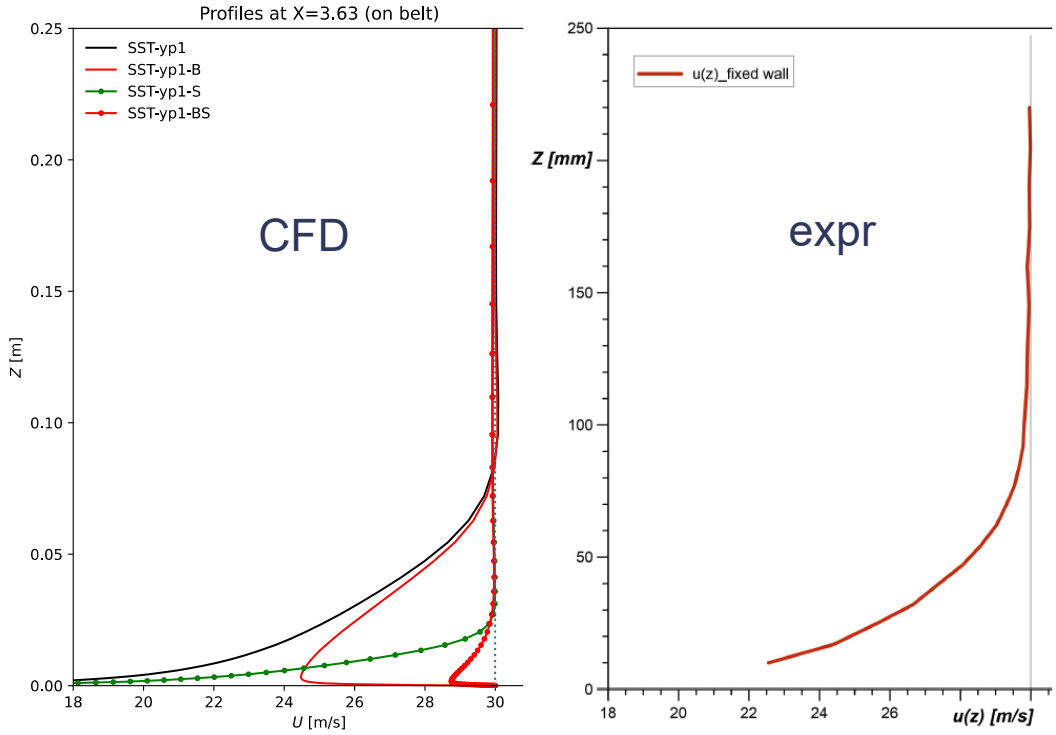

Fig. 3: Comparison of the boundary-layer profile between CFD (left, black line) and experiment (right) for the empty wind tunnel without suction and no running belt. CFD results also show the corresponding profiles for running belt (legend "B"), with suction ("S"), and combinations

Fig. 4 shows the velocity distribution in the cross direction illustrating the effect of the edge of the running belt at $y = \pm 500$mm. The wind tunnel setup introduces more disturbances compared with CFD most likely due to imperfections between the belt and the wall. In CFD the belt is assumed to have zero thickness.

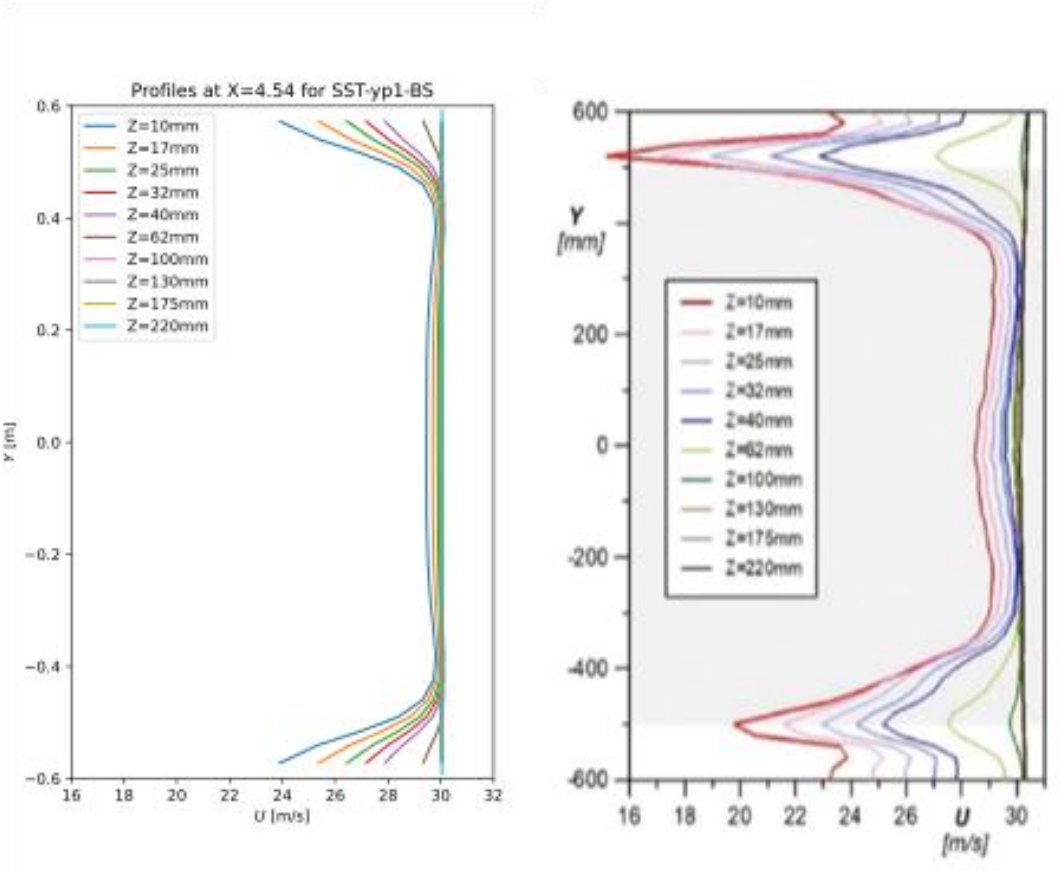

Fig. 4: Boundary-layer profiles for CFD with suction and running belt (left) compared with experiments (right). The figure pair to the left shows the velocity and the pair to the right the streamwise rms u_{rms} values

Fig. 5 shows the pressure distribution along the wind tunnel wall. The boundary layer growth along the walls results in an area contraction and acceleration of the free-stream flow which is seen as a negative pressure gradient. The different CFD results compare well with the measured acceleration, which is fairly independent of the suction and running belt except for that the suction is generating a local pressure disturbance.

The suction boundary condition is sensitive to adjust for the correct suction mass flow, which might pose problems concerning repeatability when the different train configurations are to be introduced. Moreover, some numerical difficulties were noticed. For these reasons, an artificial inlet slip wall was defined as a proxy for the boundary-layer suction. In Fig. 6 the velocity profiles and turbulence level through the boundary layer is shown. Both U and u_{rms} are well captured by CFD. It is verified in Fig.

6 that the slip wall has a similar effect on reducing the inlet boundary layer. In fact, the setup with the slip wall is somewhat closer to the measured profiles. It was decided to use the inlet slip for the following studies of the different train configurations installed in the wind tunnel.

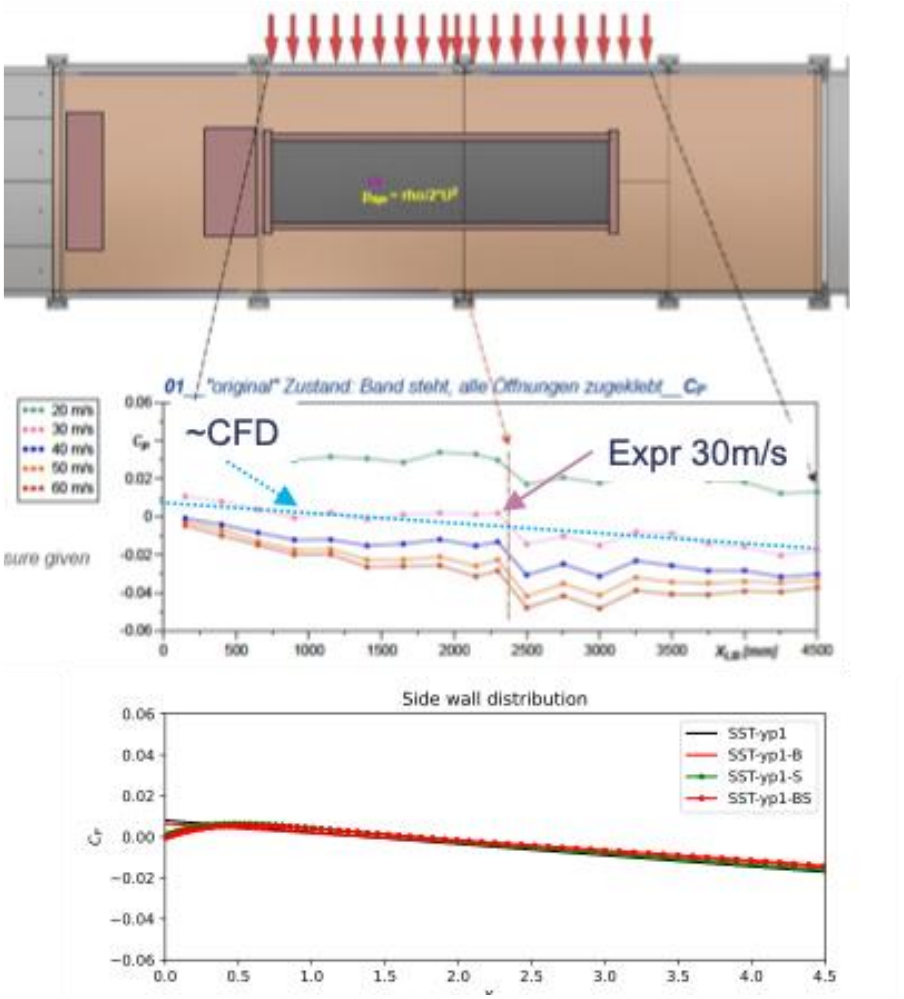

Fig. 5: Pressure distribution along the wind tunnel. CFD with different combinations of belt and suction compared with measurements

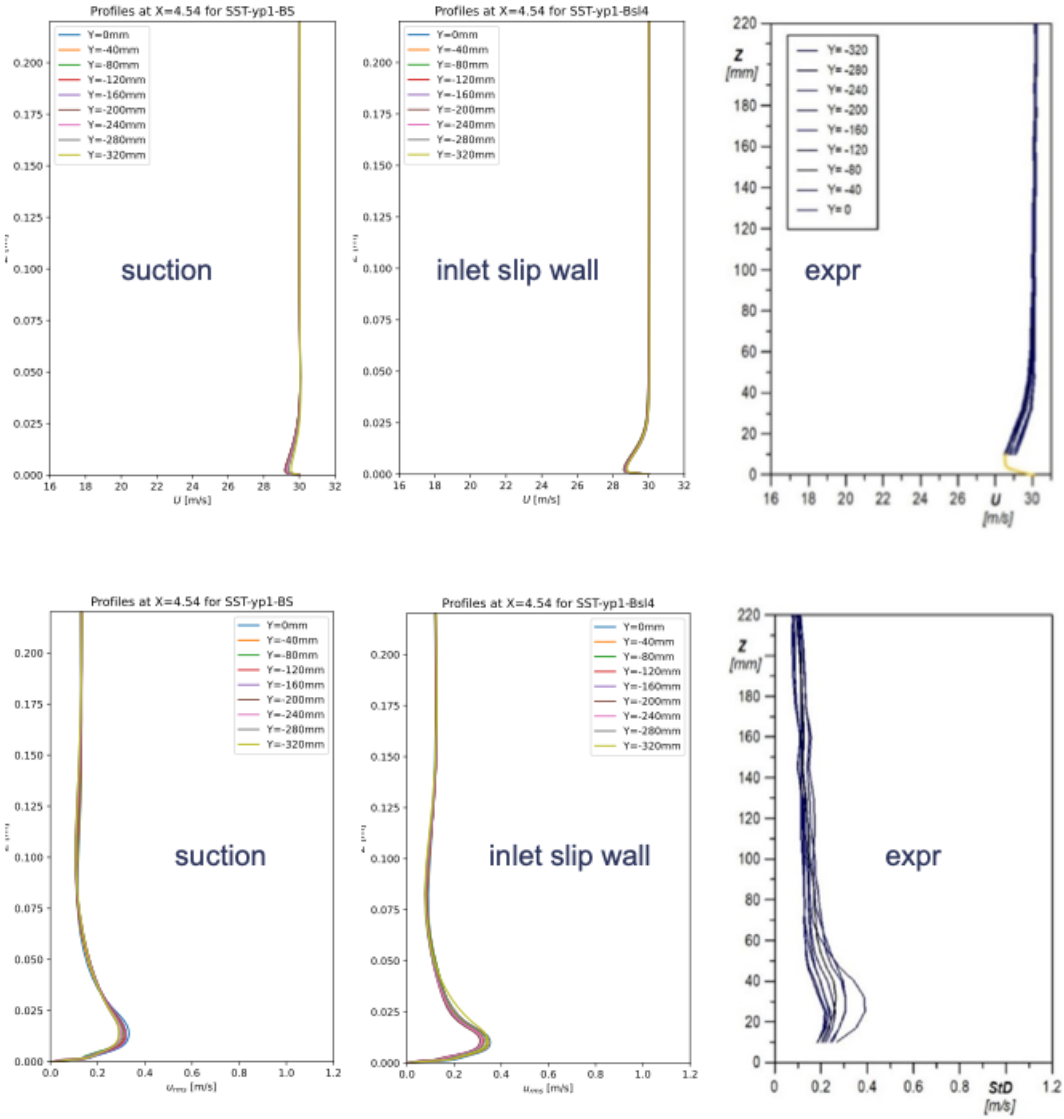

Fig. 6: Boundary-layer profiles for CFD with suction panel (left) and slip wall (middle) compared with experiments with suction and running belt (right). Velocity (top row) and turbulence u_{rms} (bottom row)

7.4. Domain of Numerical Simulations in the Wind Tunnel

The CFD domain will be constrained by the wind tunnel geometry. Several wind tunnel geometries with different grades of complexity have been suggested and provided by DLR for CFD simulations. Among the available options the following two have been reviewed:

- **Wind tunnel EdC | WT_C.** Simplified wind tunnel geometry composed by nozzle and test section, with a sliding patch to control the boundary layer thickness and a projection of the moving belt surface, shown in Fig. 7.

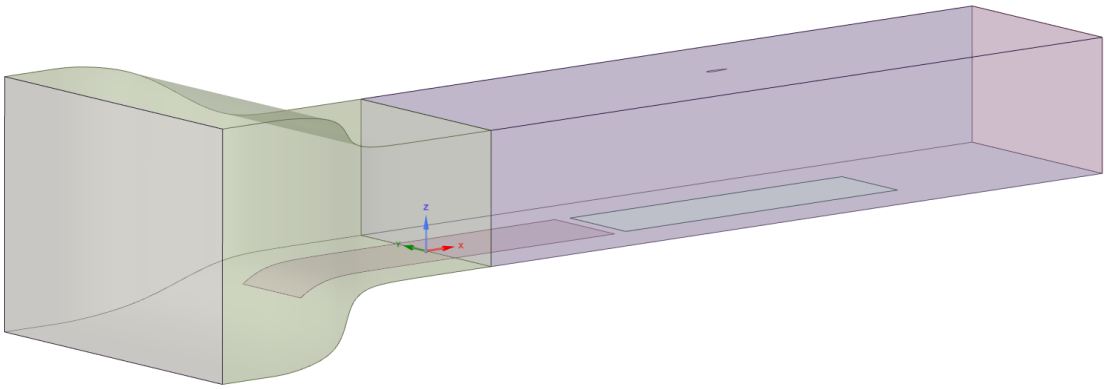

Fig. 7: WT_C domain for CFD simulations

- **Wind tunnel EdD | WT_D.** Most complete wind tunnel geometry composed by nozzle, test section and diffuser (see Fig. 8). Additionally, the moving belt geometry and the two (passive and active) boundary layer suction mechanisms have been included.

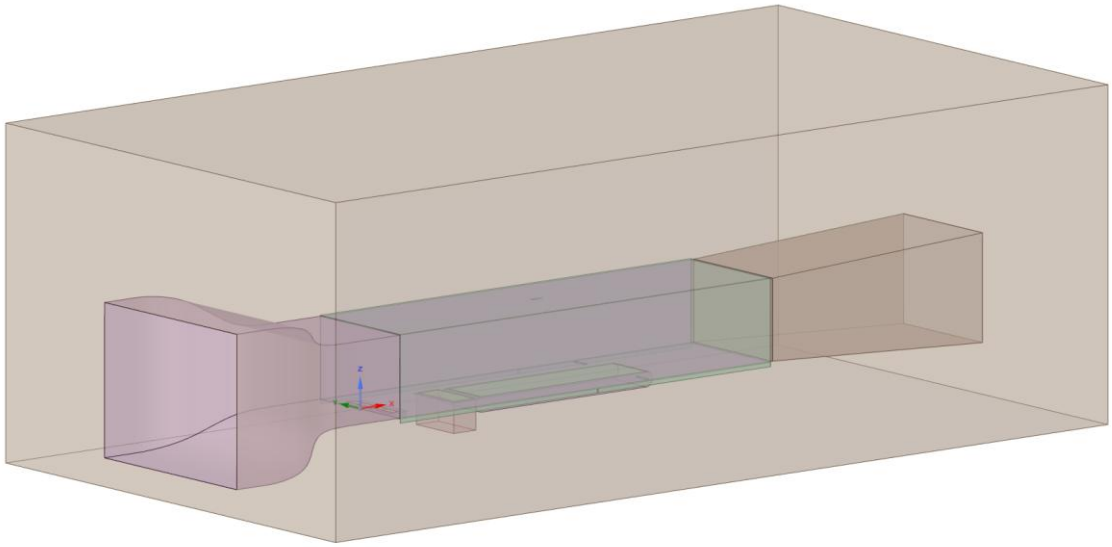

Fig. 8: WT_D domain for CFD simulations

For this first iteration, the simplified **WT_C** geometry has been considered for CFD simulations based on the conclusions from the previous section. This geometry has the following distinctive features (see Fig. 9):

- **Contraction nozzle** – located upstream the test section where the upcoming airflow will be directed to the tested vehicle

- **Test section** – In this part, both the tested vehicle and the moving belt will be located
- **Slipping patch** – friction free Surface (approximating the suction panel)
- **Moving belt** – projection of moving surface inside the test section

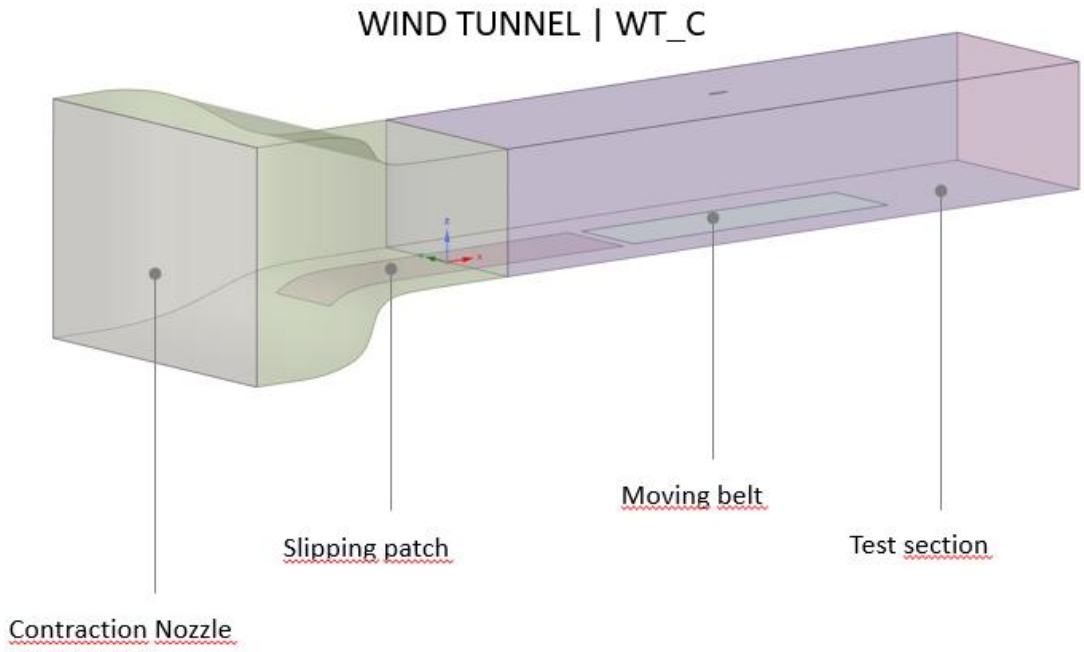

Fig. 9: Main characteristics of WT_C domain for CFD simulations

The main reason for choosing the C model over the D model is its simplicity, which is an advantage for its adjustment and configuration. However, if problems/limitations related to the domain definition are observed during the analysis of results, actions will be taken to correct them. If this does not occur, the intention is to keep domain C due to its simplicity.

7.5. Vehicle model

The tested train model is named as KMF train, which was already presented in the last report. KMF train has two main distinctive features:

- It is a **fictional train** and thus, its geometry does not exactly match any specific train in particular. However, it is a **generic geometry** with many common aspects with the **conventional trains** that can be found in the market.
- The **design is modular and customizable**, which allows a wide variety of options to be tested after some minor adjustments. This is very convenient for the wind tunnel test campaign.

In this first iteration, 5 different KMF geometries have been considered for CFD simulations:

- **KMF_C01.** Fictional continuous & smooth geometry.
- **KMF_C02.** Equivalent to C01 with a flat roof to install equipment. No roof-side fairings.
- **KMF_C03.** Real train geometry including coupler, snowplough, bogies and intercommunication. However, no roof side fairings and no roof equipment are included.
- **KMF_C04.** Equivalent to C03 with roof side fairings. Still no roof equipment.
- **KMF_BG.** Geometry KMF_C01 including bogies only.

A description of the different geometries can be observed in the following Fig. 10.

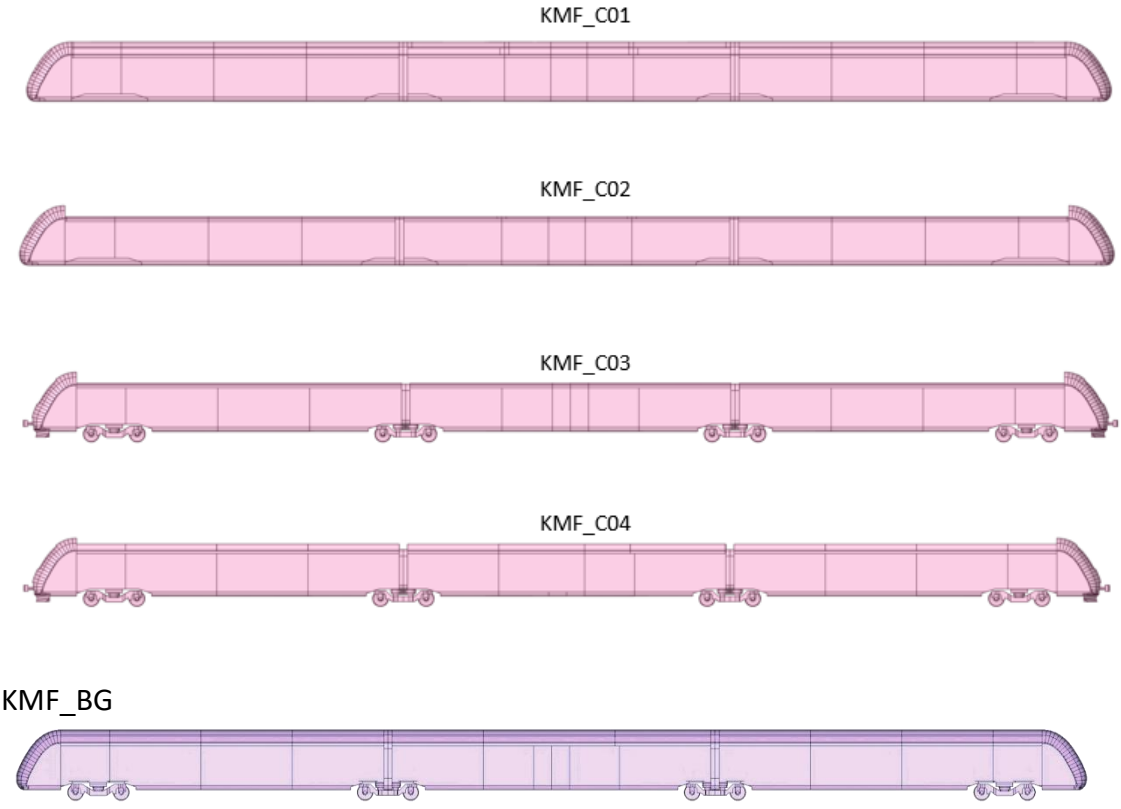

Fig. 10: Considered KMF geometries for CFD simulations

As can be seen from the sequence described in the image above, the geometry gains complexity with each iteration. The more simplified versions (C01, C02, C03) are of informative interest and are used as a prelude to check if there are problems in convergence and numerical stability, to move towards C04 in case no problems are

observed. The C04 geometry will be the first to be tested in the wind tunnel and therefore the first to offer the possibility of comparing CFD to wind tunnel results. Moreover, the KMF_BG configuration was added to study the effect of the bogies only.

7.6. Overall Boundary Conditions

Boundary conditions are defined as follows in Fig. 11.

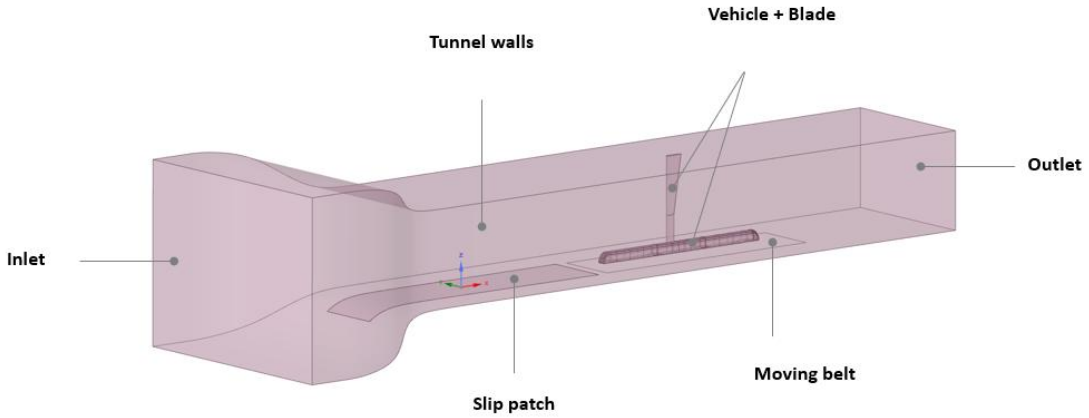

Fig. 11: Boundary conditions of the wind-tunnel domain as well as the train and mounting

- **Inlet.** Fixed inlet velocity that will be adjusted to obtain the required air velocity in the test section. KTH used a total state inlet.
- **Outlet.** Surface where the reference pressure is defined. In this case - P_outlet: 0 Pa. KTH used a fixed mass-flow rate to obtain the required air velocity in the test section.
- **Tunnel walls.** Fixed surface with no slip condition.
- **Vehicle + Blade.** Fixed surface with no slip condition.
- **Slip patch.** Surface with slip condition. This is a frictionless surface to account for the suction mechanisms that control the boundary layer build up. Its size and position with regard to the vehicle are used as a control mechanism to obtain an equivalent boundary layer thickness on the test section.
- **Moving belt.** Surface with no slip condition moving at an imposed velocity. The moving velocity of this surface will be equal to the airflow in the test section

The boundary conditions applied by KTH is somewhat different concerning the in/out flow boundaries mainly due to that KTH is using a solver for compressible flows.

7.7. Mesh

The mesh strategy has been divided into different steps:

- As a first step to **setup the mesh** of the wind tunnel, **empty wind tunnel simulations** have been performed. The main objective of these simulations is to establish a good correlation for **velocity profile at fixed position inside tunnel** when wind tunnel and CFD results are compared
- Once a good correlation for the inlet velocity profile has been obtained at the measurement position inside the tunnel, the **mesh** has been **updated** to **include the simulated vehicle**. The position of the studied vehicle shall be equivalent to the one on the wind tunnel.

7.7.1. Empty wind tunnel

Empty wind tunnel air speed is available at x=4.54 m (provided by DLR) for different heights. The origin of coordinates (X,Y,Z = 0,0,0) is placed at the interface between the nozzle and the test section.

CFD simulations will be carried for the following purpose:

- Inlet air speed will be adjusted until the air speed inside the test section is equivalent to the one on the wind tunnel tests. Alternatively, KTH is adjusting the outlet mass flow rate.
- Errors between CFD and wind tunnel experimental velocity profile at the measured position shall be minimized
- The defined mesh shall be able to represent the upcoming airflow with sufficient accuracy. Important velocity gradients shall be captured and sufficient resolution shall be available to complete the previous two steps

The approximation of the suction panel by an inlet slip wall is validated, discussed and motivated by KTH in the previous section.

Additionally, CAF tested **two different mesh approaches** for the empty wind tunnel simulations. The difference between them lies on the **refinement zone** one of them has above the moving belt. The main features of the mesh can be summed up as follows in Fig. 12.

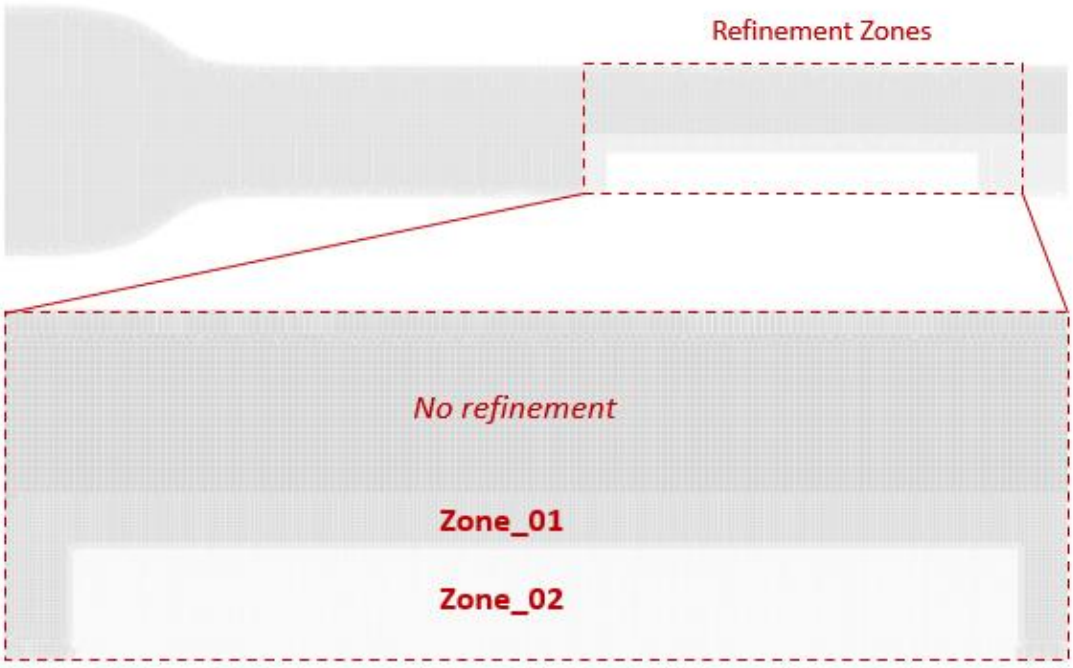

Fig. 12: Refinement zones inside the volumetric mesh

Since the different actors involved in simulation activities may have slight variations in the definition of the mesh size, mesh element or simulation software, all the main parameters have been summed up in the following table Tab. 2.

The meshing strategy for KTH is somewhat different where the mesh is built bottom up from basically structured surface patches refined locally near the different interfaces. The idea when adding the train model is to let the train drive the necessary resolution in the wind tunnel as well.

Tab. 2: Mesh parameters of the different numerical methods

	CAF		Hitachi/PoliMi		KTH	
	Mesh_01	**Mesh_02**	**Mesh_01**	**Mesh_02**	**Mesh_01**	**Mesh_02**
Meshing software:	ANSYS Meshing	ANSYS Meshing	-	SnappyHexMesh (openFOAM)	Fidelity Pointwise (Cadence)	Fidelity Pointwise (Cadence)
Mesh type	Polyhex	Polyhex	-	hex-dominant	hex-dominant	hex-dominant
Cell number:	3588078	40061691	-	42855946	1.7M	2.4M
Min cell size [m]:	0.004	0.004	-	0.004	0.006	0.006
Max cell size [m]:	0.032	0.032	-	0.032	0.1	0.1
Boundary layer | N_layers:	10	10	-	8	40	65
First layer height [m]:	0.0008	0.0008	-	0.0008	0.01e-3	0.2e-3
Growth rate:	1.2	1.2	-	1.5	1.15	1.15

Average y+:	30	30	-	30	0.7	14
Refinement zone:	No	Yes	-	Yes	No	No
Element size [m] | Zone_01	-	0.016	-	0.016	-	-
Element size [m] | Zone_02	-	0.004	-	0.004	-	-

***Note.** Mesh_02 includes two refinement zones above the moving belt for the CAF approach

7.8. Wind tunnel & KMF simulation results

Based on empty wind tunnel CFD results, the meshing approach with the refinement zone has been used as a **reference** for the next step. On the next step the vehicle has been introduced inside the wind tunnel (see Fig. 13).

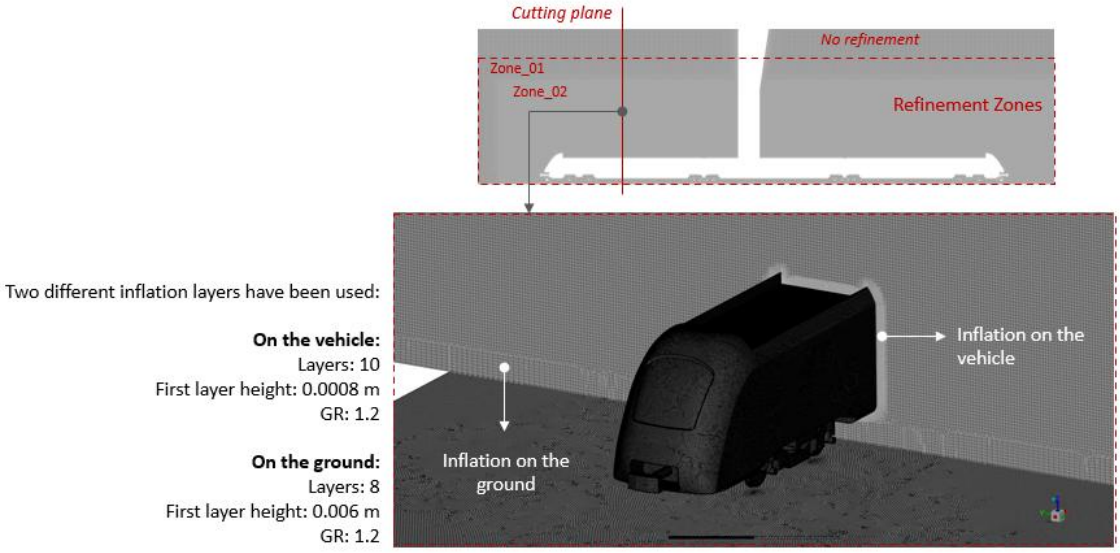

Fig. 13: Volumetric mesh characteristics with KMF vehicle inside the wind tunnel

The mesh size changes according to the simulated vehicle model. The greater the vehicle model detail the larger the mesh size. However, the overall characteristics of the mesh do not change.

Following the structure of the previous chapter a summary of the volumetric mesh for each of the involved actors is included in the following lines.

7.8.1. Wind tunnel & KMF meshing strategy by KTH

KTH is taking a somewhat different approach for the meshing considering efficiency (accuracy for given CPU effort) and accuracy for delta effects by a modular approach described in some details below.

A modular hybrid mesh is made using Pointwise. The surface mesh on the major smooth parts of the train is structured with mostly quad cells through the boundary layer. Moreover, the near field around the train is basically structured for the best trade-off between accuracy and resolution. The near field is forming a “box” with the train contained as can be seen in Fig 14. Different parts can be exchanged within this box, such as resolved bogies or covered with smooth surfaces. Moreover, the different cars are meshed separately and can be assembled in different configurations to form a complete train set. Hence, the effect of different local changes, e.g. roof configurations, can be assessed with high accuracy while keeping the rest of the mesh fixed.

Fig. 15 illustrates some more details of the mesh around the sword junction. The unstructured surface patch around the sword can be replaced by a structured block without the sword for assessing the influence of the sword.

The far field outside of the box is then added as either the resolved wind tunnel or the open field. The resolution of the wind-tunnel walls and the far field is much coarser, except in the wall-normal directions, since the flow is varying slowly along the walls away from the train. Since the meshing of the train within the box is kept fixed, the influence of the wind-tunnel effects can be assessed with higher accuracy eliminating spurious effects from remeshing just by replacing the far-field mesh. The modular meshing strategy for assembling the clean train is illustrated in Fig. 16. For example, the smooth bogie can be replaced by the part with the resolved bogie shown in the figure.

The general mesh size is 2-5mm on the train surface and in the near-field with the larger size (5mm) in the streamwise direction. Wall normal resolution for all parts of the train is 0.01mm (for $y^+ \approx 1$) and 0.2mm for all wind-tunnel walls and also the sword. The expansion (growth) coefficient is 1.15 resulting in 13 to 16M grid nodes for all the different cases. The mesh parameters are given in the tables Tab. 3, 4 and 5.

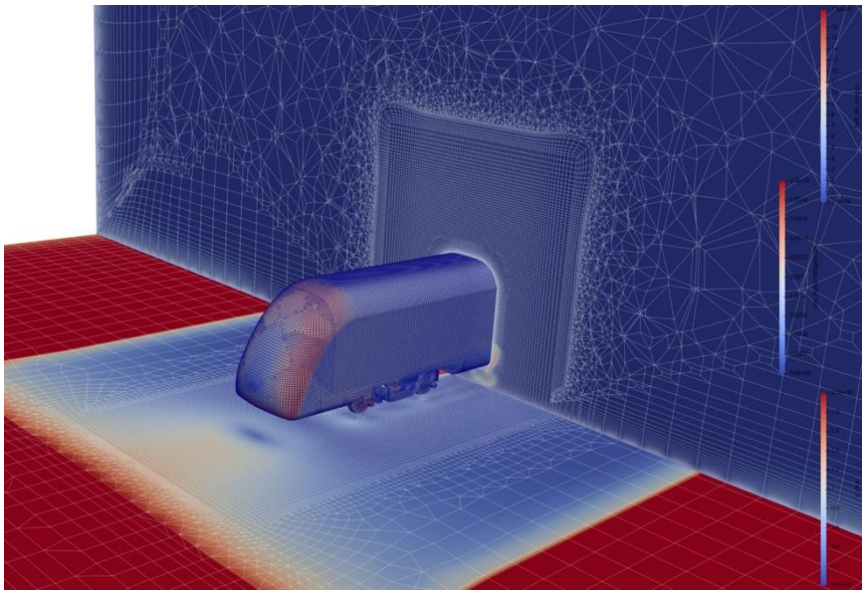

Fig. 14: Illustration of the mesh around the front head

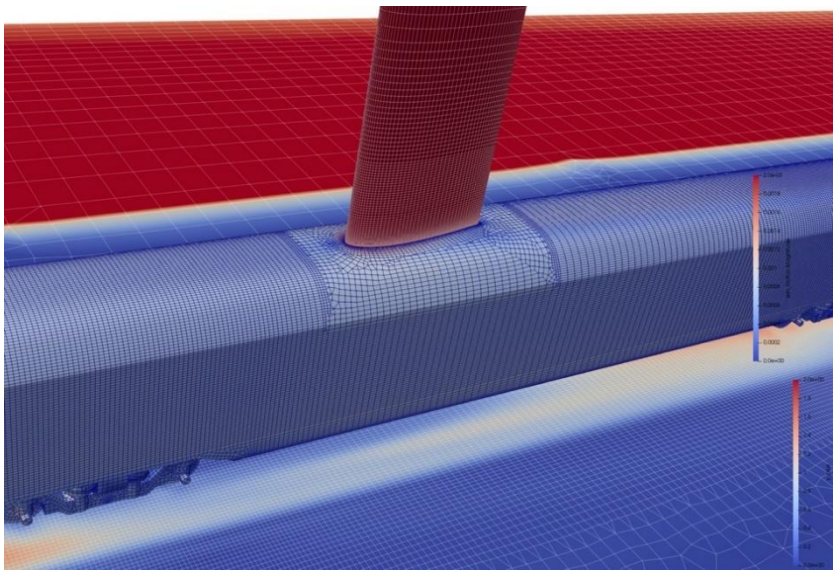

Fig. 15: Illustration of the mesh around the sword

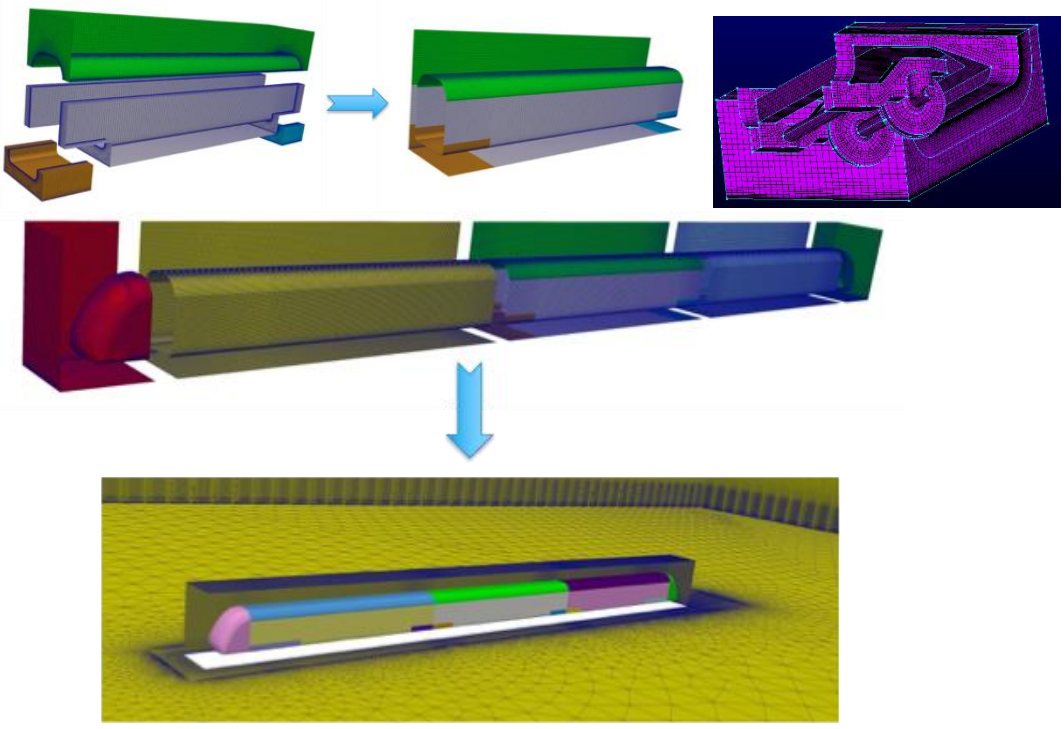

Fig. 16: Illustration of the modularized meshing. Assembling one car (top) and the complete train set (bottom)

Tab. 3: Mesh parameters used with CAF method

	Mesh | KMF_C01	Mesh | KMF_C02	Mesh | KMF_C03	Mesh | KMF_C04
Meshing software:	ANSYS Meshing	ANSYS Meshing	ANSYS Meshing	ANSYS Meshing
Mesh type	Polyhex	Polyhex	Polyhex	Polyhex
Cell number:	73.7 e06	118.4 e06	122.1 e06	125.1 e06
Min cell size [m]:	0.001	0.001	0.001	0.001
Max cell size [m]:	0.032	0.032	0.032	0.032
Boundary layer | N_layers:	10	10	10	10
First layer height [m]:	0.0008	0.0008	0.0008	0.0008
Growth rate:	1.2	1.2	1.2	1.2
Average y+:	30	30	30	30
Refinement zone:	Yes	Yes	Yes	Yes

Element size [m] | Zone_01	0.016	0.016	0.016	0.016
Element size [m] | Zone_02	0.004	0.004	0.004	0.004

Tab. 4: Mesh parameters used with Hitachi/PoliMi method

	Mesh | KMF_C01	Mesh | KMF_C02	Mesh | KMF_C03	Mesh | KMF_C04
Meshing software:	SnappyHexMesh (openFOAM)	SnappyHexMesh (openFOAM)	SnappyHexMesh (openFOAM)	SnappyHexMesh (openFOAM)
Mesh type	Hex-dominant	Hex-dominant	Hex-dominant	Hex-dominant
Cell number:	46.5 e6	46.7 e6	47.2 e6	47.2 e6
Min cell size [m]:	0.001	0.001	0.001	0.001
Max cell size [m]:	0.032	0.032	0.032	0.032
Boundary layer | N_layers:	8	8	8	8
First layer height [m]:	0.0008	0.0008	0.0008	0.0008
Growth rate:	1.2	1.2	1.2	1.2
Average y+:	30	30	30	30

Refinement zone:	Yes	Yes	Yes	Yes
Element size [m] | Zone_01	0.016	0.016	0.016	0.016
Element size [m] | Zone_02	0.004	0.004	0.004	0.004

Tab. 5: Mesh parameters used with KTH method

	Mesh | KMF_C01	Mesh | KMF_C01-Sw	Mesh | KMF_BG	Mesh | KMF_BG-Sw
Meshing software:	Fidelity Pointwise (Cadence)	Fidelity Pointwise (Cadence)	Fidelity Pointwise (Cadence)	Fidelity Pointwise (Cadence)
Mesh type	hex-dominant	hex-dominant	hex-dominant	hex-dominant
Cell number:	19 e6	20 e6	21 e6	22 e6
Min cell size [m]:	0.002-0.005	0.002-0.005	0.002-0.005	0.002-0.005
Max cell size [m]:	0.1	0.1	0.1	0.1
Boundary layer | N_layers:	40 / 30	40 / 30	40 / 30	40 / 30
First layer height [m]:	0.01e-3 / 0.2e-3	0.01e-3 / 0.2e-3	0.01e-3 / 0.2e-3	0.01e-3 / 0.2e-3
Growth rate:	1.15 / 1.20	1.15 / 1.20	1.15 / 1.20	1.15 / 1.20

Average y+:	1 /20	1 /20	1 /20	1 /20
Refinement zone:	No	No	No	No
Element size [m] | Zone_01	-	-	-	-
Element size [m] | Zone_02	-	-	-	-

Note: The two different settings for the boundary-layer resolution applies for the train (y^+=1) and wind-tunnel walls (wall functions) respectively. Moreover, both cases are meshed with and without the sword (Sw).

7.8.2. Turbulence models

All the simulations of this first iteration have been performed RANS methods.

The used turbulence model is the Menter k-w SST [5]. The main reason can be summed up as follows:

- **Accuracy near wall regions.** The k-w SST model is useful to predict turbulent phenomena in the region close to the train's surface, where the highest velocity and pressure gradients occur. This is important to correctly capture the flow physics around complex geometries (such as conventional trains) and it is especially useful for aerodynamic drag simulations.
- **Handling of adverse pressure gradients.** The k-w SST does a good job predicting flows with separation and recirculation, which are common in running resistance and crosswind simulations where adverse pressure gradients happen.
- **Robustness, stability & flow performance.** The k-w SST combines the performance of the k-e model in the far field region with the accuracy of the k-w model near surface, making it suitable for simulating scenarios with different flow regimes withing the same simulation.
- **Computational cost.** RANS simulations with k-w SST models are computationally much more effective than transient simulations, which is a clear advantage, especially when several iterations are involved.

Thus, **k-w SST** model has been the chosen option for this preliminary simulation approach.

In addition, KTH has applied an explicit algebraic Reynolds stress model (EARSM) based on $K-\omega$ [6, 7] and the Spalart-Allmaras (S-A) [8] model are used.

7.9. Results of the Numerical Simulations

This section will display CFD results obtained by each of the partners involved in the simulation activities. The results presented by each partner will be organized according to the following structure:

- Empty wind tunnel results
- Wind tunnel + KMF vehicle model

A summary of the obtained results will be included at the end of the section.

7.9.1. CAF simulation method

7.9.1.1. Empty wind tunnel

As previously explained empty wind tunnel simulations are used to ensure a good correlation of the velocity profile acting on the tested vehicle. The performed CFD simulations with empty tunnel yield the results shown in Fig. 17.

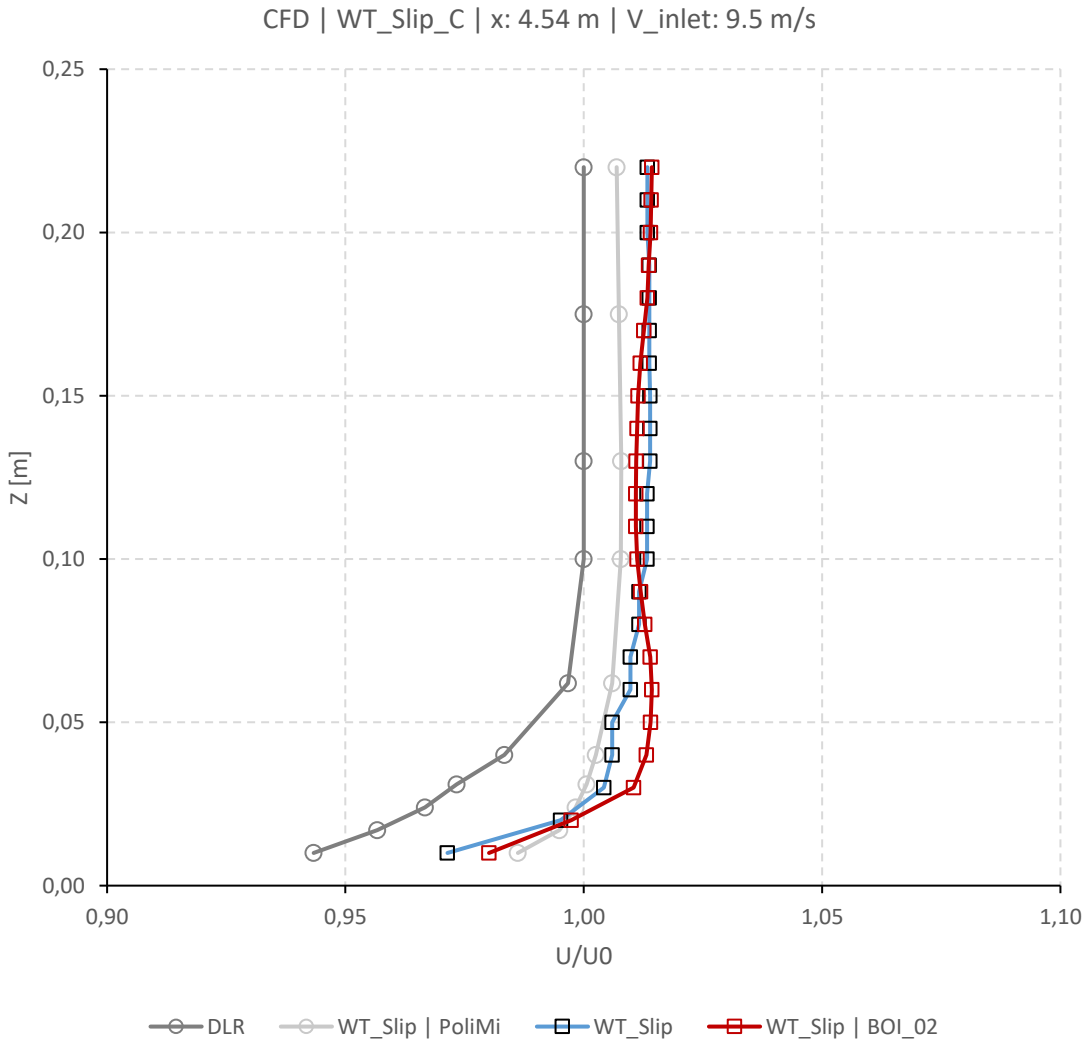

Fig. 17: Velocity profile comparison at x: 4.54 m from the origin of coordinates. DLR (Test) – CAF & Hitachi/PoliMi (CFD)

Interpretation of the obtained results:

- A comparison of the velocity profile has been done at x: 4.54 m (see section 7.7.1 for the position of [X,Y,Z] = [0,0,0]). Test results provided by DLR have been used as a reference for the comparison. Additionally, obtained CFD results have been compared to the ones obtained from Hitachi/PoliMi.

- Inlet speed has been set at 9.5 m/s to achieve a flow speed of 30 m/s in the test section (contraction section accelerates the flow).
- U/U_0 has been computed at different heights. The air speed has been normalized using 30 m/s as a reference speed (U_0)
- According to the obtained results it can be concluded the flow speed at the test section (x: 4.54 m) is slightly over 30 m/s (+1-2%)
- The deviation of CFD results with regard to wind tunnel results are always below 5% at any measurement point (below 2% above 60 mm)
- The results are consistent* with other CFD approaches (see Hitachi/PoliMi), although the CAF's approach with a refinement zone shows a slight overspeed bubble for heights between 30 mm and 80 mm

***Note.** CAF reports wind profile speed as the average value (μ) of the RANS simulation whereas Hitachi/PoliMi reports it as $\mu + 2\sigma$

Although there might be some margin to improve CFD results further, empty wind tunnel model is considered good enough to obtain a representative performance of KMF model on a first iterative step.

7.9.2. Wind Tunnel + KMF vehicle model

CFD simulation results for all the simulated vehicle models are summed up in the following table Tab. 6.

Tab. 6: Drag Fx [N] with CAF method

	Car_01	Car_02	Car_03	**Total**
BOI_KMF_C01	1.90	0.83	2.99	**5.72**
BOI_KMF_C02	2.47	0.79	4.65	**7.91**
BOI_KMF_C03	4.99	1.22	4.83	**11.04**
BOI_KMF_C04	4.90	1.21	4.63	**10.74**

The obtained forces are for the simulated vehicle model at a reduced scale (1:20), thus, not full-scale forces. Simulations up to 5000 iterations have been performed. The shown results correspond to the average of the last 2000 iterations where a statistically stable result has been achieved (see Fig. 18).

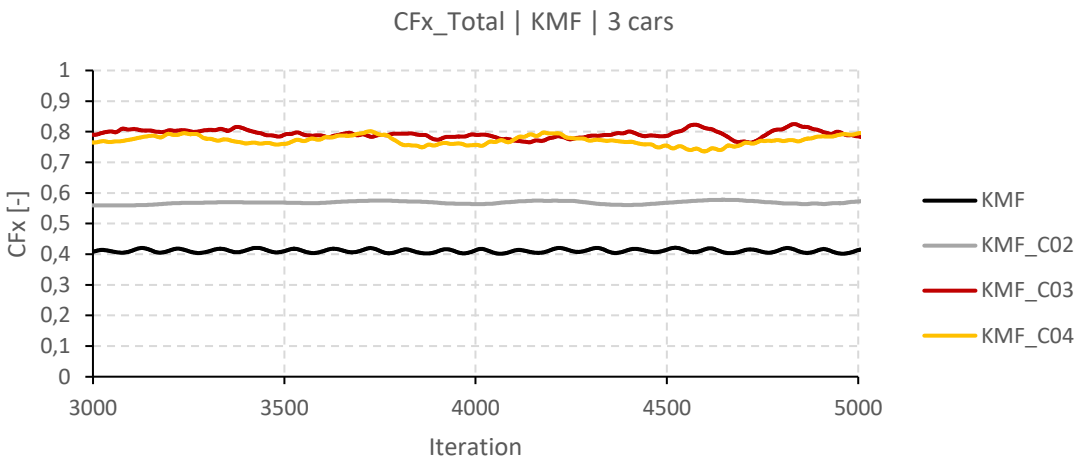

Fig. 18: Last 2000 iterations for the computed CFx on the studied vehicles (CAF-method)

Additionally, the force coefficient (CF_x) has been obtained too and is stated in Tab. 7.

Tab. 7: Force Coefficient CFx (CAF method)

	Car_01	Car_02	Car_03	**Total**
BOI_KMF_C01	0.14	0.06	0.21	**0.41**
BOI_KMF_C02	0.18	0.06	0.33	**0.57**
BOI_KMF_C03	0.36	0.09	0.34	**0.79**
BOI_KMF_C04	0.35	0.09	0.33	**0.77**

The coefficients have been obtained according to the following equation:

$$C_{Fx} = \frac{F_x}{\frac{1}{2}\rho v_a^2 A}$$

Where:

ρ: 1.205 $[kg/m^3]$

v_a : 30.4 $[m/s]$

A: 10 $[m^2]$ in full scale

***Note.** Scale corresponds to (1/20). Coefficients have been normalized using an air speed of 30.4 m/s, which is the value of the air speed in the test section according to CFD results.

In addition to the already shown results, aerodynamic drag is often obtained according to the convention set up by the Davis equation to describe the running resistance. Following that convention the running resistance can be described as:

$$R = A + B \cdot v + C \cdot v^2$$

Where the aerodynamic drag is usually associated to the C coefficient of the Davis equation and can be defined as ($^{F}/_{v^2}$). Post-processing the obtained results according to this convention leads to the results given in Tab. 8.

Tab. 8: Post-processed Results Fx [N] (CAF-method)

	Car_01	Car_02	Car_03	**Total**
BOI_KMF_C01	0.06	0.03	0.10	**0.19**
BOI_KMF_C02	0.08	0.03	0.16	**0.26**
BOI_KMF_C03	0.17	0.04	0.16	**0.37**
BOI_KMF_C04	0.16	0.04	0.15	**0.36**

This is a useful parameter when results are compared against free field on-track tests at full scale which usually follow this convention as defined on the EN14067-4 (see [3]).

Wind tunnel setup only allows to measure the force for the entire unit and therefore, forces cannot be obtained for each individual car. However, CFD simulations allow a more detailed analysis of the obtained results (shown in Fig. 19).

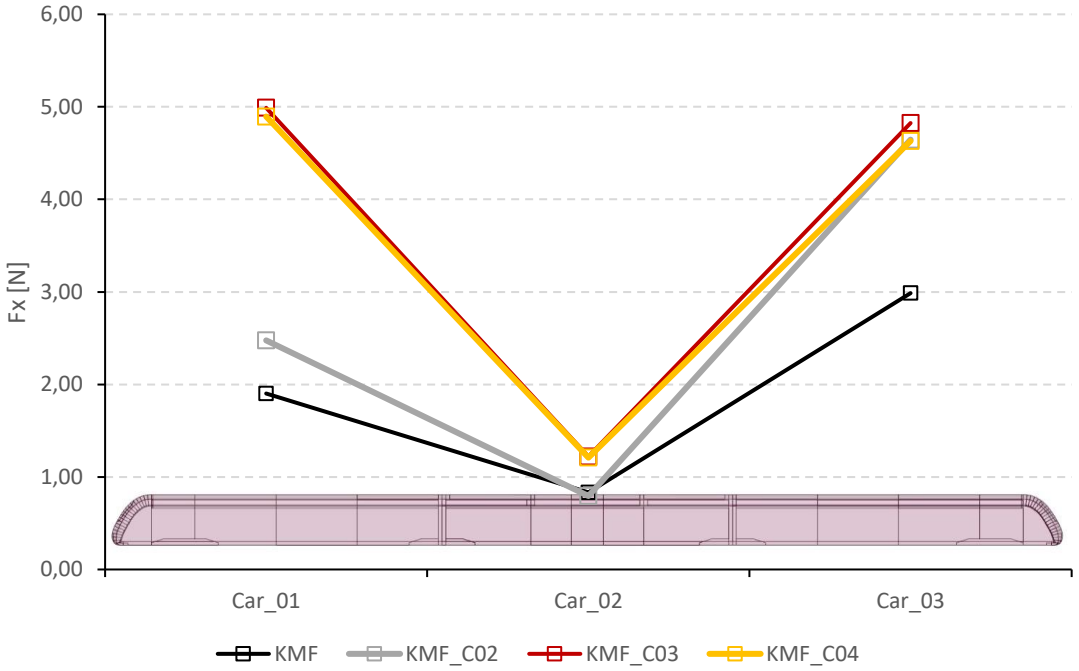

Fig. 19: Fx per car in each of the simulated configurations (CAF method)

According to the obtained results:

- Front and rear cars are the ones with the higher drag force.
- The drag force for car 01 and 03 is almost equivalent except for the smooth configurations (C01 & C02) where the trailing car's drag is higher.
- The drag of the smooth configurations (C01 & C02) is much lower than the one for non-smooth units (C03 & C04). Discontinuities on the cross section such as snowplough, bogies, fairings and intercommunication have a very remarkable impact on the drag increase.

Vehicle configurations C03 and C04 allow a more detailed assessment where the contribution of each group component to the total drag can be studied. The results obtained with these configurations are given in Tab. 9 and Fig. 20.

Tab. 9: Results of Vehicle Conf. C03 and C04 (CAF method)

	KMF_C03		KMF_C04	
Group	Fx [N]	Fx [%]	Fx [N]	Fx [%]
Bellow	0.062	1%	0.063	1%
Bogie	0.857	8%	0.827	8%
Cab	5.650	51%	5.441	51%
Car	2.68	24%	2.68	25%
Coupler	0.17	2%	0.18	2%
Snowplough	1.61	15%	1.55	14%
Total	**11.037**		**10.737**	

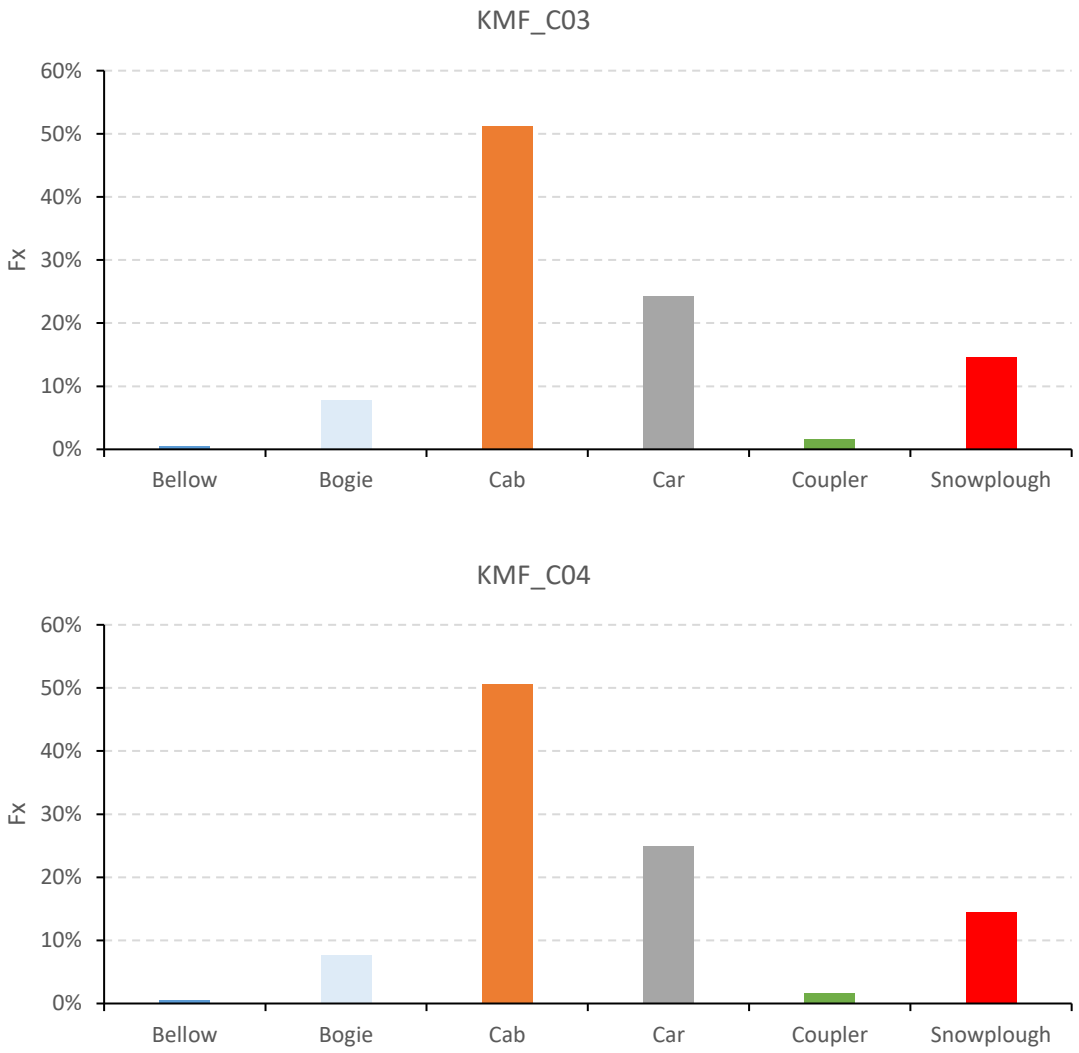

Fig. 20: Contribution of different components to the overall drag force (Fx) (CAF method)

According to the obtained results:

- The biggest contributor to the overall aerodynamic drag is the cab geometry with a contribution around 50% of the total drag. In vehicles configurations with a low number of cars (3 in this case) a short head shape (which is usually the case for conventional vehicles) has a very important contribution to the drag force.
- The next biggest contributors are the carbody and the snowplough with a 25% and a 15% respectively
- It has to be acknowledged that on these preliminary calculations no roof equipment has been considered so far which will clearly influence drag contribution

7.9.3. Hitachi/PoliMi

7.9.3.1. Empty wind Tunnel

The empty wind tunnel results obtained by Hitachi/PoliMi numerical simulations have already been presented in section 7.9.2. The inlet conditions are the same of CAF's simulations. The deviation from the wind speed of the experiments and the numerical result is in the order of 1%.

7.9.3.2. Wind Tunnel + KMF vehicle model

The force results of the CFD analysis on the 1:20 train model are given in the table Tab. 10.

Tab. 10: Force Results Fx [N] of PoliMi Simulations

	Car_01	Car_02	Car_03	**Total**
KMF_C01	1.98	0.93	2.63	**5.54**
KMF_C02	2.55	0.89	4.50	**7.94**
KMF_C03	4.90	1.30	5.01	**11.21**
KMF_C04	4.90	1.30	5.11	**11.31**

As for CAF's simulations, 5000 iterations have been performed and the results are the average of the last 2000 iterations where a statistically stable result has been achieved (see Fig. 21).

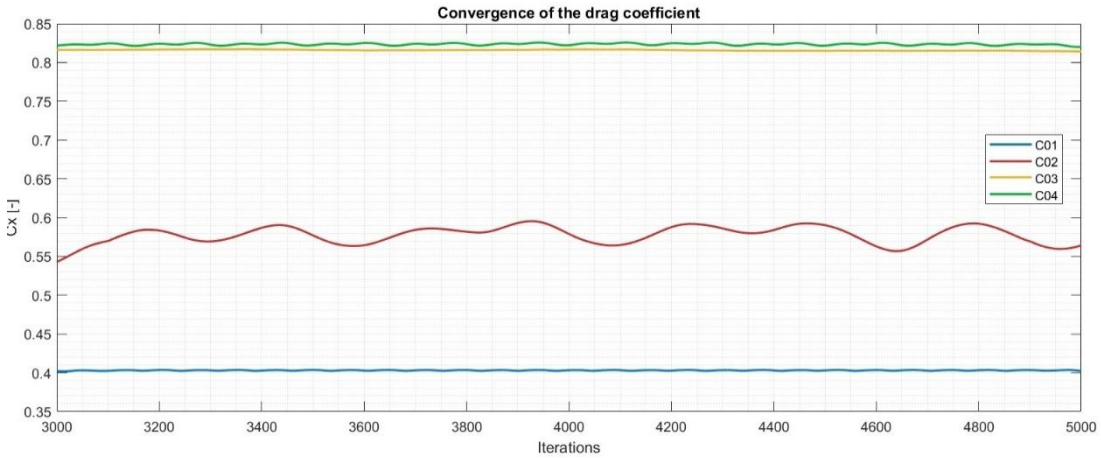

Fig. 21: Last 2000 iterations of the force coefficients (Hitachi/PoliMi)

The force coefficients derived from the simulations are presented in the following table Tab. 11.

Tab. 11: Force Coefficients of PoliMi Simulations

	Car_01	Car_02	Car_03	**Total**
KMF_C01	0.144	0.068	0.191	**0.403**
KMF_C02	0.186	0.065	0.323	**0.578**
KMF_C03	0.357	0.095	0.364	**0.816**
KMF_C04	0.357	0.095	0.372	**0.824**

The coefficients are obtained using the speed of the reference point in position x = 2.5 m, y = 0 m, z = 1 m, in proximity to the tip of the pitot tube of the wind tunnel (see Fig. 22). The air speed at this specific location is for all the configurations u = 30.2 m/s.

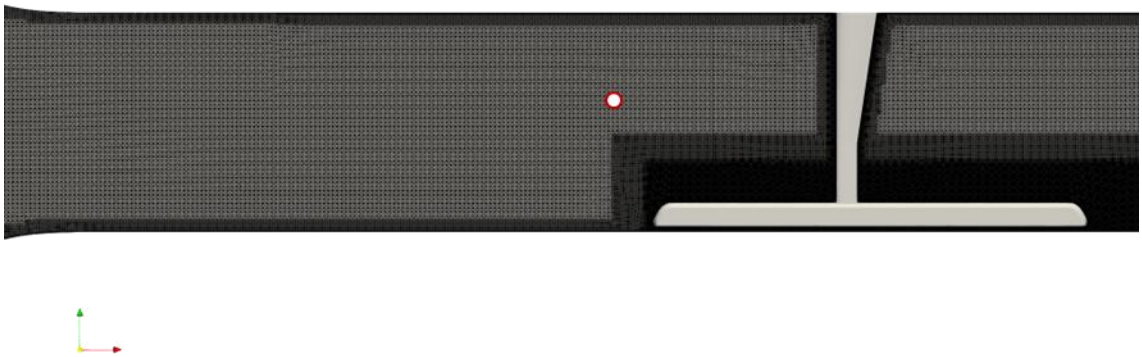

Fig.22: Reference point in the computational domain

Analysing the drag coefficient for sections along the train model length it is possible to find out the relevance of certain features of the geometry on the overall aerodynamic resistance. This is pictured in Fig. 23. and Fig. 24.

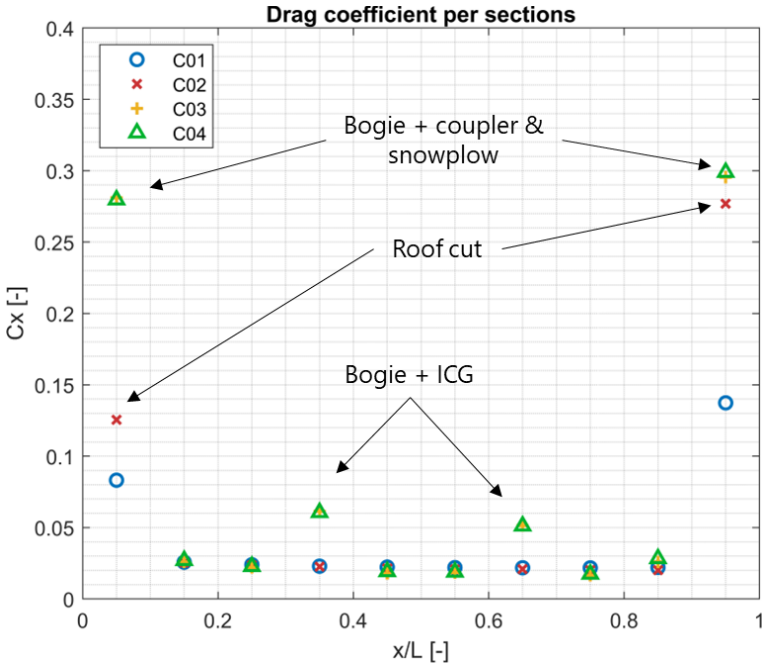

Fig. 23: Drag coefficient divided per sections along the length of the train

Overall, the highest drag contribution is given by the tail of the train model, regardless of the configuration.

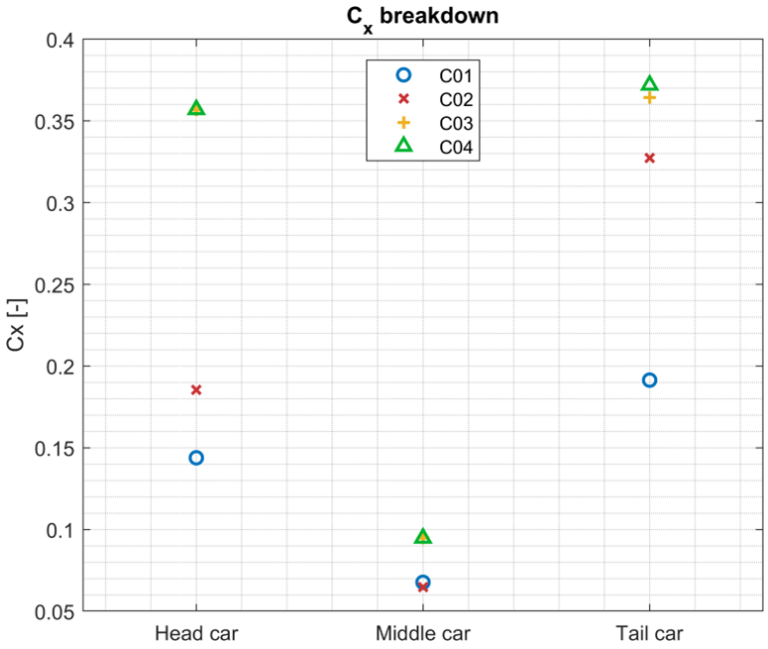

Fig.24: Drag coefficient for train cars

7.9.4. Results obtained by KTH method

Two train configurations have been studied so far. These are the clean train with closed bogies and the clean train with resolved bogies, see Fig. 25. The configurations with open roof and different roof configurations will be considered for the next study. Both configurations have

been computed both with and w/o sword within the wind tunnel. They are computed in open ground conditions at both wind-tunnel and full-scale Reynolds numbers. Hence, in total 8 configurations. Moreover, both configurations with sword in the wind tunnel have been computed with three different RANS models and the open-field configurations have been computed with non-zero side slip as well. Some additional test runs with short configurations without the mid car have been performed as well but will not be reported here.

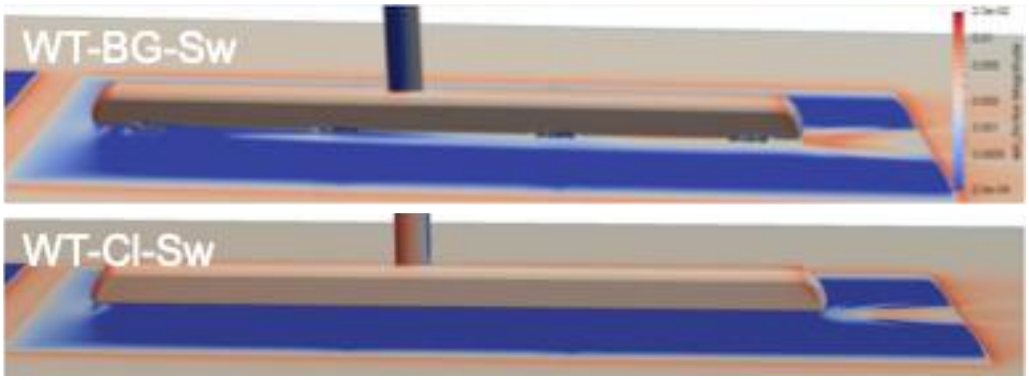

Fig. 25: Illustration of the two basic configurations studied by KTH

The force and pressure coefficients are normalized by the reference condition at (x, z)=$(-1.88, 0.89)$ in the train coordinate system (in the centre of the test section just upstream of the belt).

$$C_D = \frac{\overline{F} \cdot \hat{x}}{A_{ref} q_{ref}}, \qquad q_{ref} = \frac{1}{2}\rho_{ref} U_{ref}^2, \qquad \overline{F} = \int_S [(p - p_{ref})\hat{n} + \overline{\tau_w}]dA,$$

where $\hat{x}$ and $\hat{n}$ are the direction of the x-axis and the surface normal and $\overline{\tau_w}$ is the wall skin-friction vector. Moreover, the cumulative drag along the x-axis is defined as

$$c_D(x) = \int_{x_0}^{x} \frac{\overline{f}(x') \cdot \hat{x}}{A_{ref} q_{ref}} dx', \qquad \overline{f}(x) = \int_{S(x)} [(p - p_{ref})\hat{n} + \overline{\tau_w}]dA,$$

where $\overline{f}(x)$ is the local force vector at x. Hence, $c_D(x_1) = C_D$, where x_1 is at the end of the train.

One need to pay attention to the fact that C_D for an open part will be dependent on p_{ref} while a closed part such as the complete train is independent of p_{ref} due to the fact that the surface integral of a constant quantity (such as p_{ref}) is zero for a closed domain. Hence, if the reference is taken as the outlet or inlet pressure, then C_D for the individual parts will be different mainly as a redistribution of the drag between the front and rear parts. The same is for the cumulative drag, $c_D(x)$, which will have a different profile depending on the reference pressure but $c_D(x_0) = 0$ and $c_D(x_1) = C_D$ independently of p_{ref}.

The computations are run by using the M-Edge code [8, 9], which is an edge and node-based Navier-Stokes flow solver for compressible flows applicable for both structured and unstructured grids. The governing RANS equations are integrated to steady state, with a fully implicit

approach. Low-speed preconditioning is applied for the present applications. Weak boundary conditions are applied on all boundaries. The present calculations employ a second-order central discretization of the convective terms for the mean flow and turbulence transport equations with a small amount of artificial dissipation. The Menter SST $K-\omega$ model is used for most of the computations for modelling the turbulence in RANS mode. Moreover, an explicit algebraic Reynolds stress model (EARSM) based on $K-\omega$ and the Spalart-Allmaras (S-A) model are used. 2.500 iterations are made, and the solution is averaged over the last 500 and presented as the mean and rms values.

The drag coefficient, C_D, for the different setups is concluded in Figs. 26-28. In the left figures, C_D is reported for each component as well as the total excluding the sword. The rms of any fluctuations during the last 500 iterations is reported as error bars. The figures to the right show the cumulative $c_D(x)$ for the same settings. The two train configurations are the clean train with bogies resolved (label "BG") and with the bogie cove closed ("Cl"). The wind-tunnel conditions are kept for the computations with the train in the wind-tunnel ("WT") with the sword included ("Sw") or not. The same geometries and settings are applied for the train in open field conditions ("Open") including the same Reynolds number as in the wind tunnel. Finally, the open field conditions are computed with a full-scale Reynolds number ("hiRe") by a factor of 20 higher. This corresponds to the full-scale train operating at the same velocity of 30m/s and is obtained by lowering the viscosity. Scalable wall-function boundary conditions are applied keeping the mesh identical with the mesh used for the low-Re setting. Hence, the influences of the sword, the wind-tunnel installation (contraction) and the wind-tunnel Reynolds number can be quantified. These delta effects are assessed for both the clean configuration and the configuration including the bogies.

For all different settings and configurations, the mesh has been kept fixed for all parts that are not directly influenced by the change. Moreover, for the high-Re cases, the same wall-normal resolution of 0.01mm is kept by applying a universal wall-function boundary condition since the wall resolution in terms of y^+ becomes in the order of 10. Hence, the delta effects are believed to be accurately predicted. The Menter SST model has been used for most of the results.

Fig. 26 shows the influence of the different configurations. The following observations can be made

- In general, the bogies introduce a significant additional drag. The contribution mostly comes from the first car where the bogies are exposed to an energetic free-stream flow. The rearward bogies operate in thick boundary layers which reduces the drag for these.
- The viscous, or skin friction, contribution to the drag is dominant for the cars. For the clean configuration, the skin friction is responsible for the complete drag as expected.
- The drag for the forward Head A is very small.
- The trailing Head B contributes to a major part of the drag rather independently of the bogies, wind-tunnel installation or the Reynolds number. There is a rather big uncertainty of the drag for the trailing head due to unsteady flow separation manifested by large rms

values in the simulations. Moreover, RANS turbulence models are not reliable for predicting separation of thick boundary layers from a smooth surface. The skin-friction contribution to the drag of Head B is almost zero.

- The drag from the sword is quite large, but its influence on the drag for the train is minimal.
- Open field conditions give a small reduction in drag in comparison with the wind-tunnel installation.
- The high full-size Reynolds number gives a significant lower skin friction contribution to the drag. The effect is more pronounced for the clean configuration where the total drag is reduced by 0.1. For the bogie configuration the drag of the trailing Head B is increased and almost completely absorbing the reduced skin friction drag.

The delta effects are quantified in the table Tab. 12. The wind-tunnel installation effects are rather small concerning the effect of the sword, the wind-tunnel blockage, the interference with the walls and running belt.

Tab. 12: Delta effects of KMF Simulations

Delta effect, ΔC_D	**With bogies**	**Clean config**
Wind-tunnel contraction	0.03	0.02
Sword	0.00	0.00
Full-scale Re	-0.01	-0.09
Bogies for WT Re		0.23
Bogies for full-scale Re		0.30

The Reynolds-number effect is more sever though and is quite different for the clean and bogie configurations. Mostly due to that the effects through the skin-friction and pressure (separation) go in different directions. Hence, the influence of the bogies is quite different for the wind-tunnel and full-scale Reynolds numbers. This means that the influence of geometrical changes cannot be completely assessed from wind-tunnel tests only without being complimented by CFD analysis and extrapolation to full scale by CFD.

Fig. 27 shows the influence of the choice of RANS turbulence model. EARSM gives a slightly higher drag for the clean configuration (somewhat closer to the measured values) mainly by a higher drag for the rear Head B. There are almost no differences for the bogie configuration between EARSM and SST. S-A gives a general higher skin-friction drag than the other models. The drag for the sword is much higher, though, by using the S-A model. Such a large difference should not be expected and should be further examined before considered as conclusive.

Finally, Fig. 28 shows the influence of side wind computed for the open field conditions and with the ground running in the direction of the train, not in the direction of the wind as done in the wind-tunnel tests, so comparisons with wind-tunnel data is not exactly relevant. The increased AoA give rise to additional drag. For the bogie configuration we see that the rearward bogies are fed with fresh energetic wind and produce more drag for that reason. For the clean configuration, there is more drag for the rear Head B. For both configurations, the skin-friction drag increases with the angle since the boundary layer is continuously swept away.

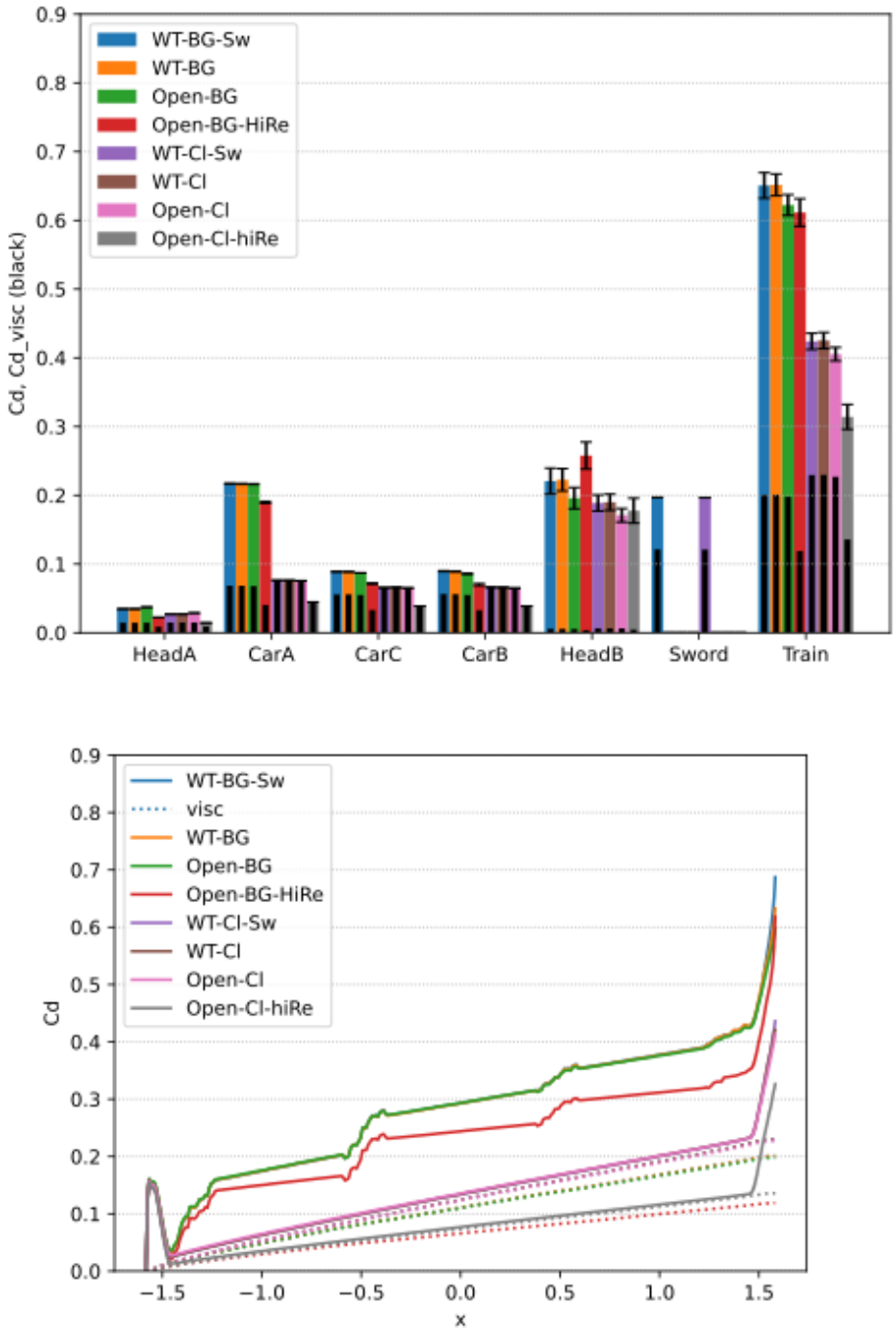

Fig. 26: Drag coefficients for different parts (top) and cumulative drag (bottom) for the two geometries in wind tunnel with and w/o sword, open field and high-Re using SST

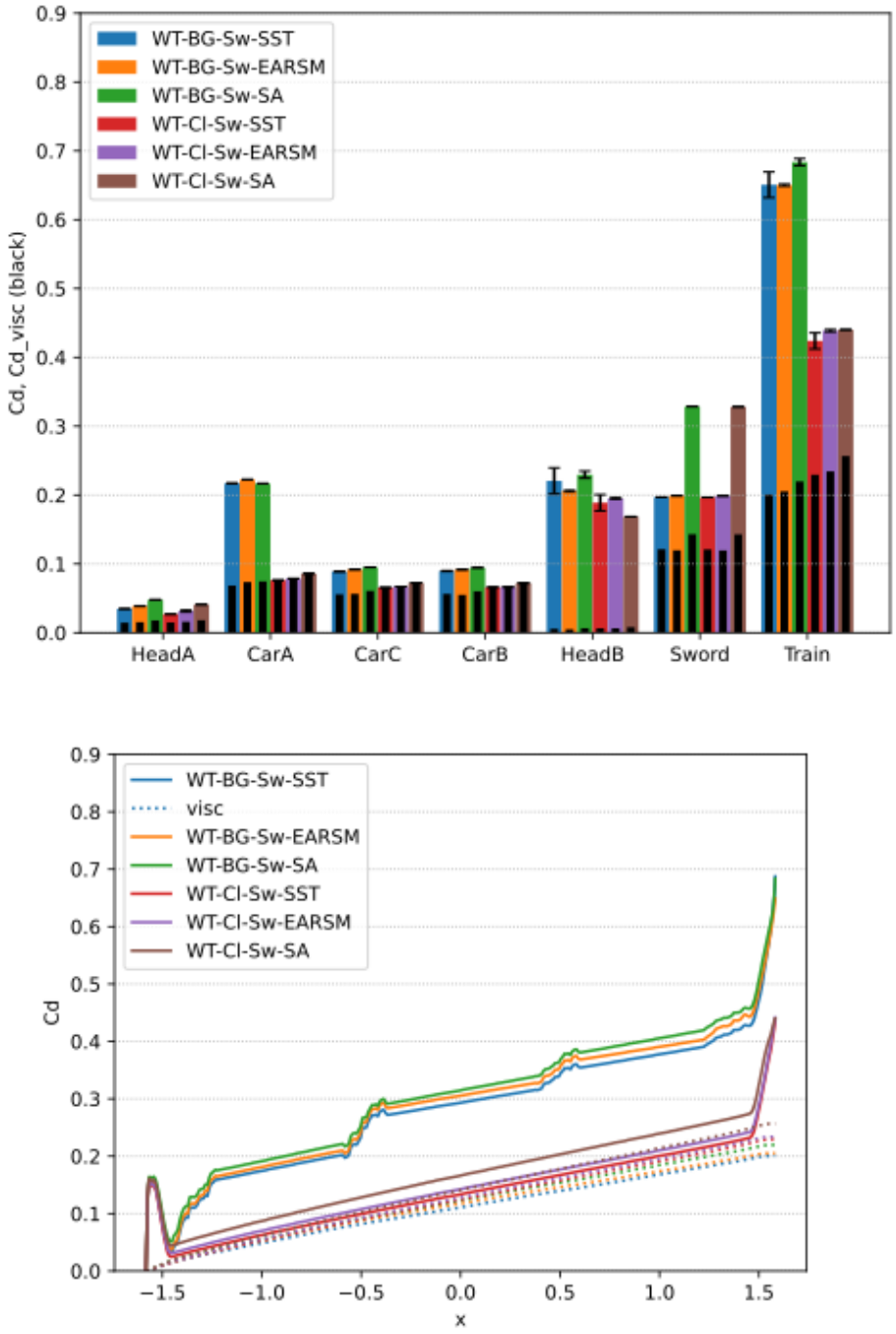

Fig. 27: Drag coefficients for different parts (top) and cumulative drag (bottom) for the two geometries in wind tunnel with and w/o sword. Influence of turbulence models

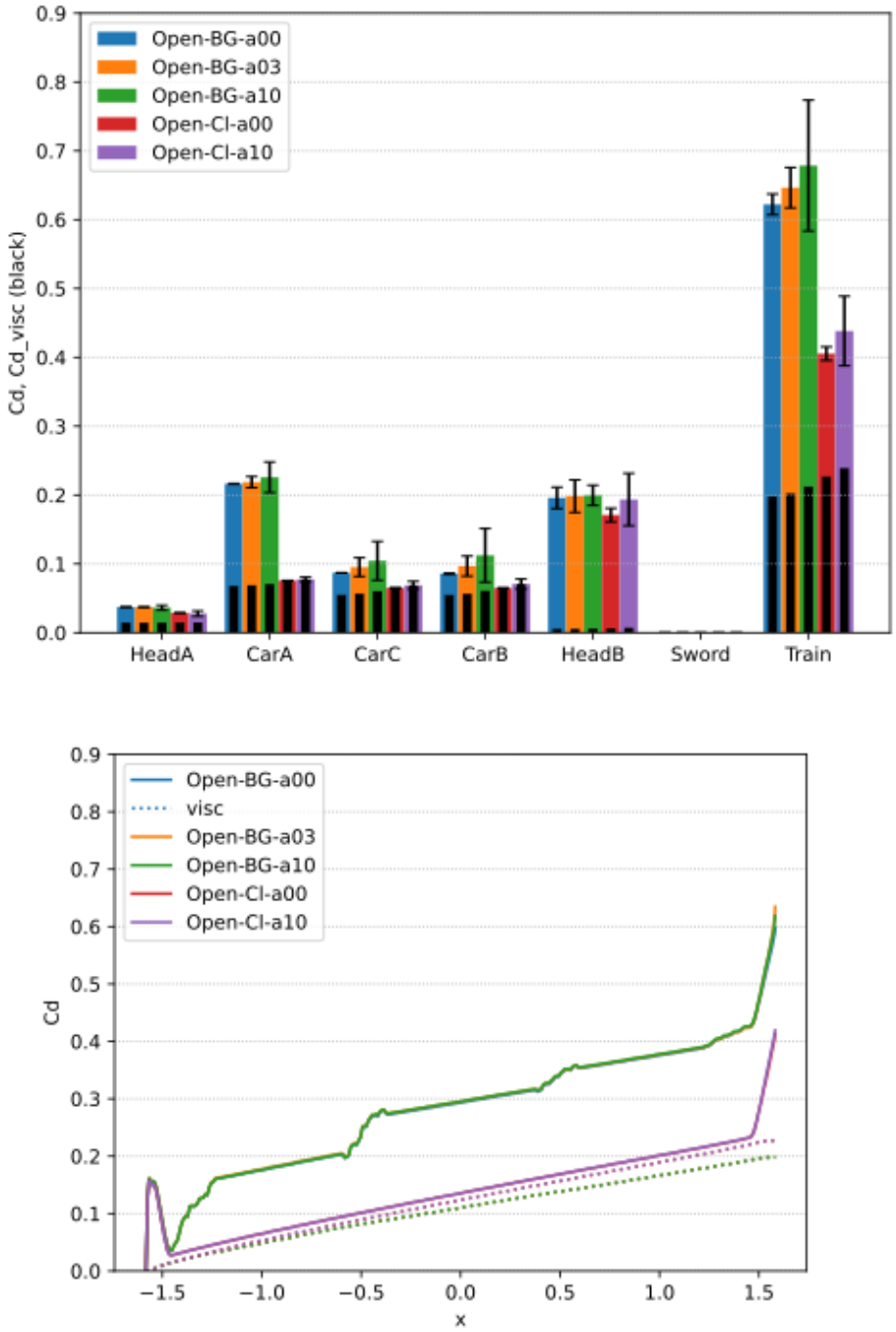

Fig. 28: Drag coefficients for different parts (top) and cumulative drag (bottom) for the two geometries in open conditions using SST. Influence of side wind

The first comparison with wind-tunnel data is shown below. It is clear that there is a rather big discrepancy between the data and the CFD simulations. From the study concluded in Fig. 38 it is rather clear that the large uncertainty comes from the rear Head B, which is also expected considering the limitations of RANS model approaches of predicting separation from smooth surfaces. The precise position of the separation is important for the aft body pressure recovery and related drag. Moreover, for the present case, the flow separation interacts with a thick, turbulent boundary layer which is another challenge for a RANS model to capture. Scale-

resolving simulations (e.g. hybrid RANS/LES) can improve the possibilities of better predictions, but they must be made with outmost care.

The drag contribution from the smooth front Head A and all cars should be discussed as well. We can see from Fig. 38 that there is a small, but systematic, difference in drag between the different RANS models. The differences would add up to about the magnitude of the difference between the measurements and CFD. Such difference between RANS models usually indicate that the case is sensitive to details. Hence, the boundary-layer tripping applied in the experiments, and possible minor wall roughness might be of importance. These details might be studied in more detail by CFD in the later part of the project.

The strategy taken by KTH for complementing wind-tunnel measurements by CFD for more reliable extrapolation to real full-scale conditions is discussed. First, the wind-tunnel itself must be sufficiently represented also in the CFD model and a careful CFD study was made mimicking the flow within the wind tunnel. For accurate assessment of delta effects, the meshing strategy was chosen to be modular where different parts can be replaced while keeping the rest of the mesh fixed. Moreover, the train set was assembled within a tight box containing all the local flow features around the train. The same fixed mesh within the train set box is then connected to a far field in form of the wind tunnel or the open field minimizing any influence of the resolution of the train near field when assessing the wind-tunnel installation effects. The train set box can be applied also in other conditions such as tunnel passages, landscape with bridges and side-wind gusts or when simulating passing trains.

7.10. Comparison to Wind Tunnel Results

The wind tunnel test campaign has begun on May 2025 at DLR facilities in Göttingen allowing a first comparison between CFD and WT. The analysis of the wind-tunnel data is ongoing, so further wind-tunnel results will be presented in the next deliverable. However, first results of the exp. wind resistance can be used to estimate the accuracy of the different numerical approaches.

So far, KMF_C01 has been tested which results are compared against CFD simulations that have been performed by CAF, Hitachi/PoliMi and KTH. CFD simulations using the SST model lead to similar results and are below WT results by almost 20%. The EARSM and S-A models computed by KTH give somewhat higher drag with an error of 12%. The overview over the numerical results compared with the wind-tunnel data is given in Tab. 13. and Fig. 29.

Tab. 13: Results with different methods compared

	CFx | KMF_C01	Error [%]
CAF	0.41	-18%
Hitachi/PoliMi	0.40	-19%
KTH SST	0.42	-16%
KTH EARSM	0.44	-12%
KTH S-A	0.44	-12%
WT | DLR	0.50	

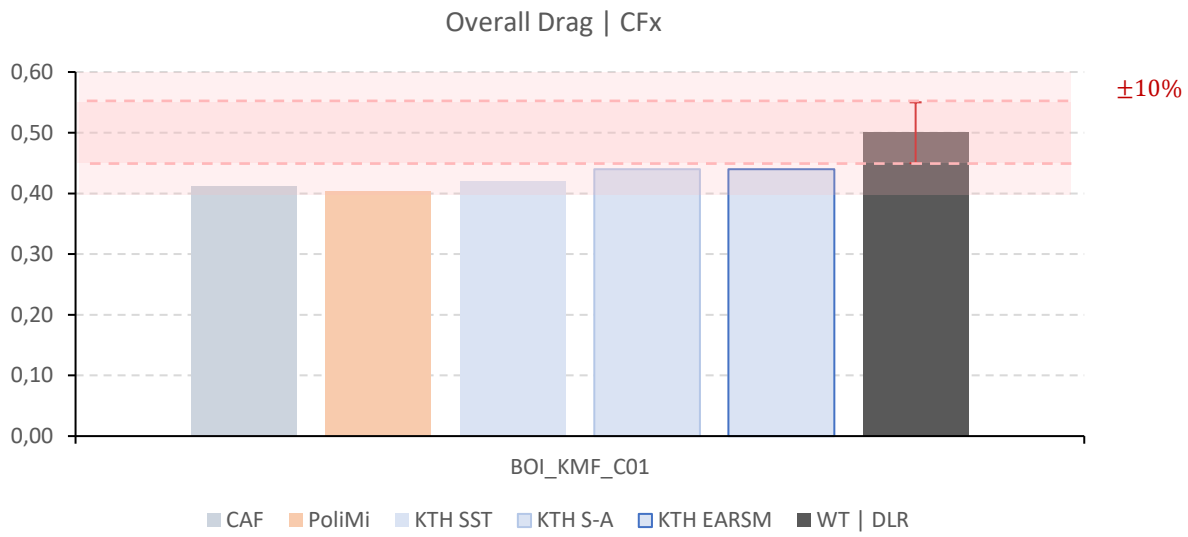

Fig. 29: CFx comparison between CFD and WT results

In this case, WT test have been performed at:

- v_{air}: $32.5\ m/s$
- ρ: $1.144\ kg/m^3$

which differ from the considered parameters for CFD simulations. Although repeatability is good on WT tests, Reynolds independency is uncertain.

According to the available results at the current stage of the project, additional iterations are necessary to improve the correlation. Furthermore, influence of the train roof complexibility on the accuracy can lead to further insight in the necessary changes in numerical techniques.

8. Conclusions and Outlook

The report sums up the work done in WP20 since the last report. The aim of the first task 20.1 of the WP is to introduce a simulation method to predict the drag and crosswind force on a train model with high accuracy but as smallest effort as possible. The second task 20.2 aims in optimizing the geometry and arrangement of the roof installations and the pantograph to reduce the drag and therefore energy consumption or to enhance the power transfer efficiency and reduce the abrasion.
Wind-tunnel tests were performed with a variety of roof configurations as well as bogie and intercar gap configurations. They contribute to both task 20.1 and 20.2.2. The analysis of the wind-tunnel tests is ongoing, so the effects of the different roof configurations on the drag will be discussed in the next report.
First wind-tunnel results as well as the results of the numerical simulations are presented in this report. To validate the simulations, the empty wind-tunnel was simulated with each of the three methods first and the flow profile was compared with the profile acquired experimentally in the SWG wind tunnel. The results show a good agreement between numerical and experimental studies. Only small deviations in shape and wind-speed variation can be determined, so the application of the methods introduced is reasonable.
For the use of the methods with train model, a variation of turbulence models was utilised to identify the best numerical setup for the given geometry configuration for each of the numerical methods. With each method, several train configurations were simulated to compare the drag of the configuration and to detect the efficiency of the method for the different geometrical setups. It can be stated, that there is a deviation between the wind-tunnel and the numerical results with regards to the drag of the train. The num. simulations predict a smaller drag than the WT results. However, the test parameters (wind speed and density) differ slightly between the WT tests and the num. simulations.
The simulations showed, that the main ratio of drag is generated at the train heads and also mounting parts like the snowplough have significant impact on the drag.
Further simulations with trains with roof installations are to be completed. The results will give insight into the flow development around the train and may lead to a clarification of the low drag in the simulations. Furthermore, a Reynolds-Number dependency can be possible which will be quantified with the help of numerical simulations adapted to the exact wind-tunnel conditions.
The ongoing work will comprise the further analysis of the wind-tunnel results obtained at DLR Göttingen with regards to the aim of task 20.2.1 as well as the completion of the experimental tests of the aerodynamic performance of the pantograph model.

The numerical simulations of the train model with roof installations will be continued and, depending on the results, the methods will be adapted to enhance the accuracy of the results.

9. References

[1]: TSI LOC&PAS: COMMISSION REGULATION (EU) No 1302/2014 of 18 November 2014 concerning a technical specification for interoperability relating to the 'rolling stock — locomotives and passenger rolling stock' subsystem of the rail system in the European Union

[2]: EN 14067-6:2018+A1:2022 Railway applications - Aerodynamics - Part 6: Requirements and test procedures for cross wind assessment

[3]: EN 14067-4:2013 Railway applications - Aerodynamics - Part 4: Requirements and test procedures for aerodynamics on open track

[4]: CEN Technical Report PD CEN/TR 17833:2022-08-15: Railway applications. Guidance for the use of simulations. Guidance for the use of simulations to demonstrate compliance with technical and regulatory requirements and on the introduction and development of simulation requirements into standards

[5]: Menter, F.R. "Two-Equation Eddy-Viscosity Turbulence Models for Engineering Applications," AIAA Journal, Vol. 32, No. 8, 1994, pp. 1598-1605.

[6]: Menter, F.R., Garbaruk, A.V. and Egorov, Y., "Explicit algebraic Reynolds stress models for anisotropic wall-bounded flows", Progress in Flight Physics 3 (2012) 89-104.

[7]: Spalart, P.R. and Allmaras, S.R., "A one-equation turbulence model for aerodynamic flows" La Rech. Aérospatiale (1994) 5–21.

[8]: Eliasson, P., Weinerfelt, P., "Recent Applications of the Flow Solver Edge", Proceedings to 7th Asian CFD Conference, Bangalore, India, 2007.

[9]: Eliasson, P., "EDGE, a Navier-Stokes Solver for Unstructured Grids", Proceedings to Finite Volumes for Complex Applications III, 2002, pp. 527-534.